

Chapter 17

Neutrino Sources and Detection of Neutrinos

17.1 Introduction

There are many sources of neutrinos in the universe. For example, neutrinos are produced inside the sun, the earth, and the entire atmosphere. Neutrinos are also produced during the birth, collision, and death of stars. Particularly huge flux of neutrinos is emitted during supernovae explosions. Most of the neutrinos that pass through the earth come from the sun and are produced in the nuclear fusion reactions going on inside the sun's core. In addition, (anti)neutrinos are produced in nuclear power plants. The beams of high energy protons striking a target material produce intense flux of pions and kaons, which then decay to produce neutrinos. There are neutrinos around us which were born almost 13.8 billion years ago,

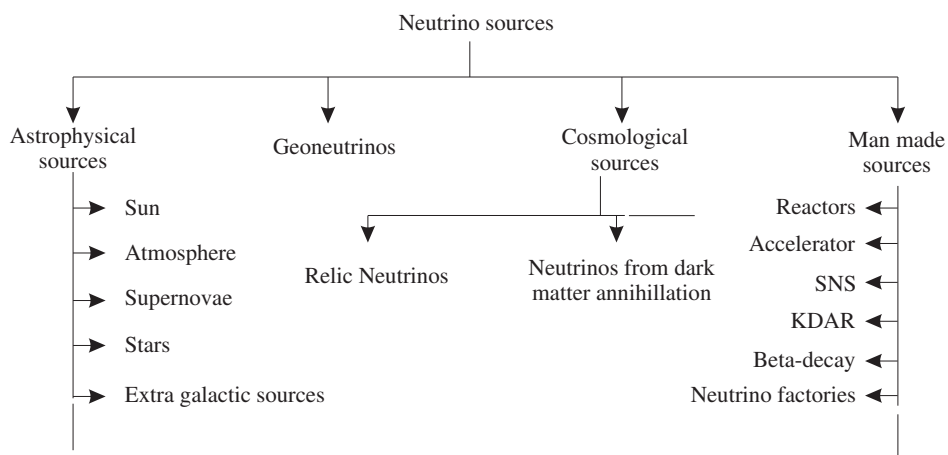


Figure 17.1 Different sources of neutrinos.

soon after the birth of the universe; they constitute cosmic neutrinos (relic of the Big Bang). Neutrinos produced inside the core of the earth are called geoneutrinos.

Figure 17.1 represents the different sources of neutrinos. Besides these sources, neutrinos are also produced by our body; they are also present in vegetables and fruits, etc. In fact, we are living in a sea of neutrinos having a wide range of energies. Simply speaking, through an area of 1 cm^2 of our body, almost a billion neutrinos pass every second. The theoretically obtained energy ranges of these neutrinos are quite broad, ranging from micro electron volts for the neutrinos left over from the Big Bang, right up to peta electron volts for the neutrinos produced in the violent gamma-ray bursts in the universe. Figure 17.2 shows the predicted neutrino flux as a function of neutrino energy from a variety of neutrino sources. Some of these neutrinos have been studied by various neutrino experiments. In this chapter, we will discuss some of the important neutrino sources and their detection techniques in various energy regions.

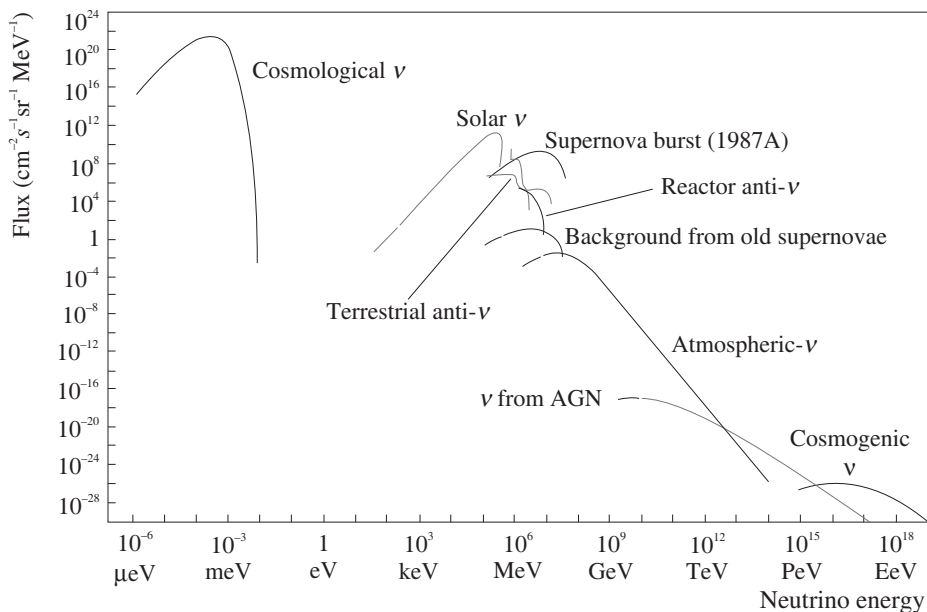
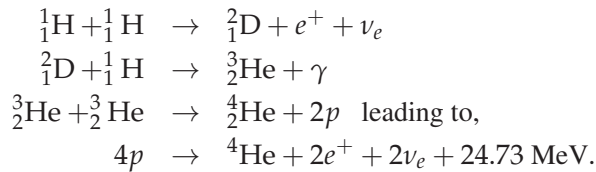


Figure 17.2 Neutrino flux as a function of neutrino energy [883].

17.2 Solar Neutrinos

17.2.1 Production

The sun is the main source of energy for the earth. It was first suggested by Eddington [884] that nuclear fusion is the source of solar energies as well as the source of energies of other stars. However, it was Bethe [885] in 1939, who explained the mechanism of thermonuclear fusion reactions, stating that hydrogen burning takes place inside the core of the sun, in which neutrinos are being produced, along with helium and positrons. The underlying nuclear fusion process is:



Finally, two positrons annihilate with the two electrons present in the solar matter, such that the reaction may be summarized as:



In other words, four protons are consumed in the production of 26.73 MeV of nuclear fusion energy. About 97–98% of the total energy released in this process is in the form of heat and light (photons). The remaining 2–3% is carried away by the neutrinos. The average energy of two neutrinos released in the aforementioned reaction is about 0.53 MeV. Since photons interact via electromagnetic interaction, after they are produced in the core of the sun, they are scattered and rescattered due to the interaction with solar matter during their passage through the sun, after they are produced in the core of the sun. It has been shown that it takes almost 10^4 years on an average, for the photons to come out of the solar core. In contrast, neutrinos, being weakly interacting particles, do not interact much with the sun's interior matter and travel almost with the speed of light; they reach the earth in about 8 minutes. Thus, neutrinos carry direct information about the sun's interior.

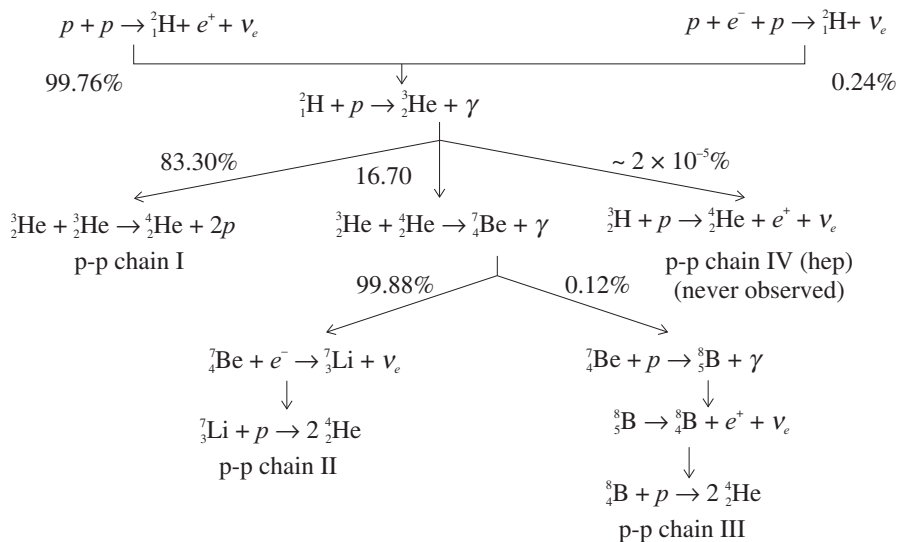


Figure 17.3 Proton–proton chain.

Solar neutrinos go through the nuclear processes driven by two different cycles of reactions, which are known as the pp (proton–proton) cycle and the CNO (carbon–nitrogen–oxygen) cycle. The pp cycle (Figure 17.3) dominates in low-mass stars and the CNO cycle (Figure 17.4) dominates in heavy stars. For example, in case of the sun, about 99% of the energy is produced

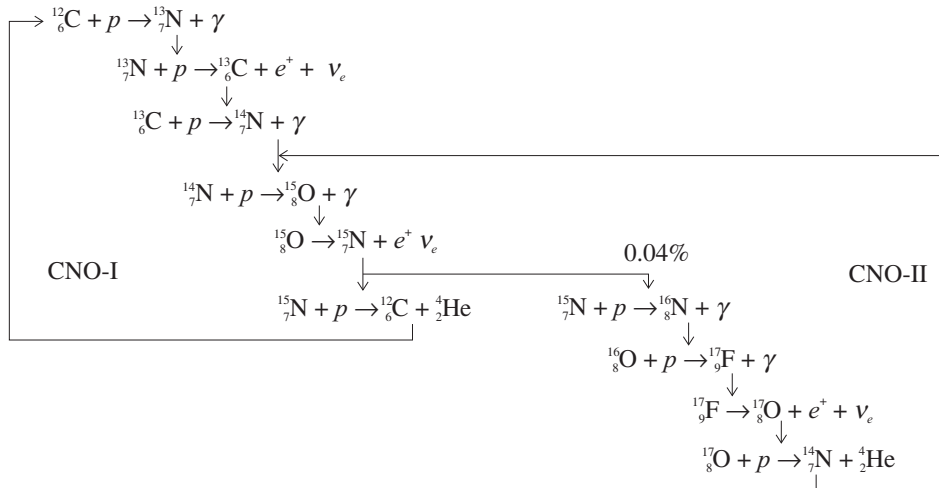


Figure 17.4 Carbon–nitrogen–oxygen cycle.

by the pp cycle. The pp cycle is quite slow in comparison to the CNO cycle. The detailed computer simulations of the electron neutrino flux, created by thermonuclear reactions in the interior of the sun, were performed by Bahcall et al. [182]. The present status of these studies, the prediction level, and the accuracy of the model is such that it has been acronymed as the standard solar model (SSM), which is basically the theory of stellar evolution. Some of its assumptions are as follows:

- The sun was chemically homogeneous at time $t = 0$.
- The initial abundance of heavy elements was the same as it is now.
- Inside the sun, nuclear fusion reactions are the only source of energy production.

The input parameters of the SSM are the initial abundance of heavy elements, radiative opacities, nuclear reaction rates, nuclear cross sections, solar age, and solar luminosity. It predicts the neutrino flux, density profile of the sun, temperature, etc. The SSM provides a good description of each component of the nuclear reaction cycle, viz., pp, pep, hep, ^7Be , ^8B , ^{13}N , ^{15}O and ^{17}F (Figures 17.3 and 17.4) which produce solar neutrinos in different energy ranges. In Figure 17.5, the energy spectrum of the solar neutrinos on the surface of the earth, predicted using the SSM, has been shown. Using the luminosity of the sun ($L_\odot = 3.826 \times 10^{26} \text{W}$), the solar neutrino flux on the earth is estimated to be about $6.47 \times 10^{10} \text{ cm}^{-2} \text{ s}^{-1}$.

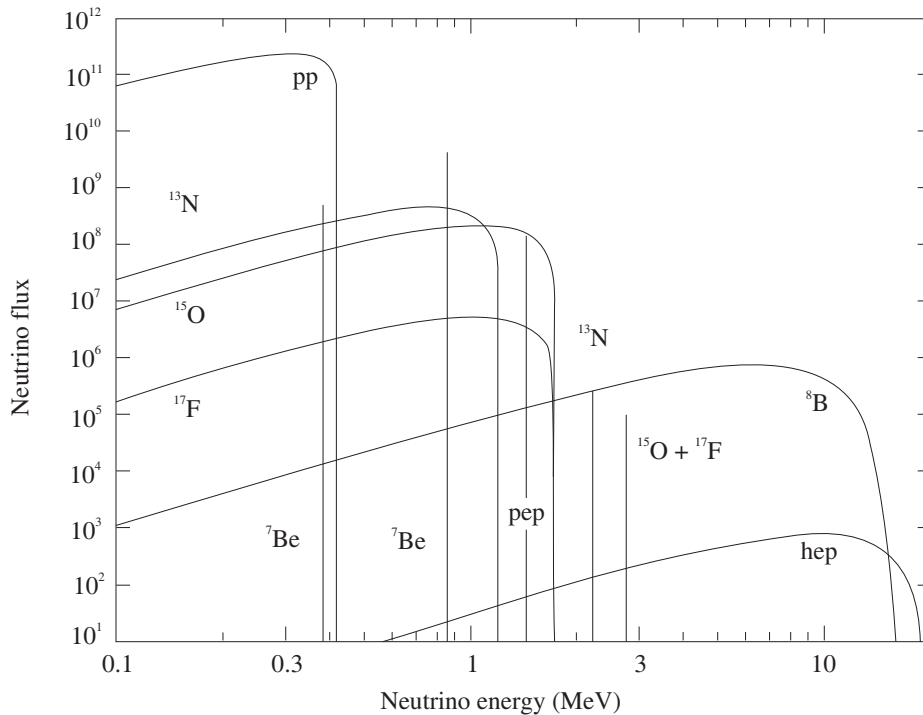


Figure 17.5 Solar neutrino spectrum in the SSM [182].

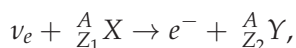
17.2.2 Detection

The $\nu_e - e^-$ cross section at 1 MeV is about 10^{-44} cm², and similarly, $\nu_e - N$ cross sections are small as discussed in Chapter 10. Therefore, to detect neutrinos, large detectors with high detection sensitivity are required. Furthermore, to avoid the background arising due to the presence of cosmic rays (mostly μ^\pm , p , and n), and which have an average flux of about 200 particles/m²/s, the detectors must be placed deep underground. Pontecorvo suggested performing a solar neutrino experiment with the reaction $\nu_e + Cl \rightarrow e^- + Ar$; however, it was not feasible when proposed. Later, Davis, Jr. and Bahcall in 1964, suggested the radiochemical experiment with solar neutrinos, which was performed by Davis, Jr. at the Homestake Mine located in a rock cavity, 4,850 feet below the surface in Lead, South Dakota. The setup had a tank filled with 100,000 gallons of tetrachloroethylene (C₂Cl₄) to detect solar neutrinos. In general, each molecule of C₂Cl₄ contains one atom of ³⁷Cl, the desired isotope; the other three chlorine atoms contain two less neutrons. When a neutrino having energy more than the threshold energy ($E_{th} = 0.814$ MeV) of the reaction strikes ³⁷Cl, it produces an atom of ³⁷Ar and an electron is released, that is, $\nu_e + {}^{37}_{17}Cl \rightarrow e^- + {}^{37}_{18}Ar$. The atoms of ³⁷Ar are allowed to accumulate for several months, and are then removed by purging the tank with helium gas. The argon is then analyzed for radioactivity (${}^{37}_{18}Ar \rightarrow {}^{37}_{17}Cl + e^- + \bar{\nu}_e$). Davis, Jr. and his collaborators reported a solar neutrino deficit which is the difference between the predicted solar neutrinos using the SSM and the observed ones. This is known as the solar

neutrino anomaly. After their experiments, several other experiments like SAGE, GALLEX, Kamiokande, SNO, etc. which were performed to study the solar neutrino flux, also agreed with the deficit observed by the Homestake experiment. The solar neutrino anomaly was one of the longest standing and the most interesting problems in particle astrophysics, because it is the only object, besides the study of helioseismology (study of the structure and dynamics of the sun), which allows us a direct view into the solar interior. In Table 17.1, we have given a summary of the various solar neutrino experiments, the target used, and the period of active data taking, etc.

Broadly, the solar neutrino experiments are categorized into three groups:

- **Radiochemical experiment:** The basic reaction is



where Z_1 and Z_2 are the atomic numbers of the two nuclei X and Y respectively. The nucleus in the final state, that is, ${}^A_{Z_2}Y$ is radioactive with a definite lifetime. The radioactivity of this nucleus is used in the detection of this reaction. The Homestake, SAGE, GALLEX, GNO experiments are radiochemical experiments.

- **Real time experiment:** The main detection method is neutrino–electron scattering, where the Cherenkov light originating from an outgoing electron is detected and analyzed. Cherenkov light is produced if a charged particle is moving with a velocity v , in a medium of refractive index n , such that, $\beta = \frac{v}{c} > 1$. The direction of the emitted light is also correlated with the direction of the incident neutrinos. Kamiokande, Super-Kamiokande, SNO etc. are real time experiments.
- **Organic liquid scintillator experiment:** A liquid scintillator is a mixture of an organic base solvent like pseudocumene (C_9H_{12}), linear alkyl benzene ($C_nH_{2n+1} - C_6H_5$, where $n = 10 - 13$), etc. and flour. Flour is used to achieve light emission. Neutrinos are detected in a charged current interaction of ν_e with a ^{12}C target, which is naturally contained in the scintillators. In the future, for next generation neutrino experiments, the plan is to use liquid scintillators based on water. The KamLAND, a liquid scintillator detector, although meant for detecting reactor antineutrinos, measured solar neutrino fluxes from 8B and 7Be sources in 2011 and 2014, respectively.

The threshold energies for radiochemical experiments are much lower than real time experiments (Table 17.1). The thresholds for real time experiments are high due to the presence of large environmental background caused by natural radioactivities (uranium, thorium, etc.) as well as the presence of spallation products (β -unstable nuclei like ^{16}N , ^{12}N , etc.) produced by cosmic ray muons. Therefore, to observe solar neutrinos, radiochemical experiments like GALLEX, GNO, etc., which have lower energy threshold, are preferred. However, if one has to understand the deficit in 8B neutrino spectrum, due to the MSW (Mikheyev–Smirnov–Wolfenstein) effect (Chapter 18), then the real time experiments become important as the MSW effect not only distorts the 8B neutrino spectrum, but also produces ν_μ and ν_τ , to which radiochemical experiments are not sensitive. This is due to the high energy threshold for

charged current (CC) reactions induced by ν_μ and ν_τ , which is not possible in the case of solar neutrinos. However, in a real time experiment, through neutral current (NC) interactions, one should be able to observe the reaction:

$$\nu_i + A \rightarrow \nu_i + A',$$

where $i = \mu, \tau$, and A' is produced and detected in real time.

Table 17.1 shows the deficit of solar neutrinos observed in many experiments. However, it was the Sudbury Neutrino Observatory (SNO), using a real time Cherenkov detector, with 1000 tons of heavy water (D_2O), which clearly demonstrated the deficit of solar neutrino flux; the deficit was clearly proven by observing charged and neutral current processes simultaneously in the reactions:

$$\nu_e + {}^2_1D \rightarrow e^- + p + p, \quad E_{th} = 1.442 \text{ MeV(CC)}, \quad (17.2)$$

$$\nu_i + e^- \rightarrow \nu_i + e^- \text{ (ES)}, \quad (17.3)$$

$$\nu_i + {}^2_1D \rightarrow \nu_i + n + p, \quad E_{th} = 2.225 \text{ MeV(NC)}, \quad (17.4)$$

where $i = e, \mu, \tau$. ES stands for elastic scattering. The neutrino fluxes were observed to be:

$$\Phi^{CC} = \left(1.76^{+0.06}_{-0.05}(\text{stat})^{+0.09}_{-0.09}(\text{syst}) \right) \times 10^6 \text{ cm}^{-2} \text{ s}^{-1}, \quad (17.5)$$

$$\Phi^{ES} = \left(2.39^{+0.24}_{-0.24}(\text{stat})^{+0.12}_{-0.12}(\text{syst}) \right) \times 10^6 \text{ cm}^{-2} \text{ s}^{-1}, \quad (17.6)$$

$$\Phi^{NC} = \left(5.09^{+0.44}_{-0.43}(\text{stat})^{+0.46}_{-0.43}(\text{syst}) \right) \times 10^6 \text{ cm}^{-2} \text{ s}^{-1}, \quad \text{giving} \quad (17.7)$$

$$\frac{\Phi^{CC}_{\nu_e}}{\Phi^{NC}_{\nu_e, \nu_\mu, \nu_\tau}} = 0.340 \pm 0.023^{+0.029}_{-0.031}, \quad (17.8)$$

$$\frac{\Phi^{CC}_{\nu_e}}{\Phi^{ES}} = 0.712 \pm 0.075^{+0.045}_{-0.044}. \quad (17.9)$$

It was found that Φ^{NC} , which was sensitive to all the three flavors of neutrinos, closely agrees with the predictions of SSM, while Φ^{CC} , which was sensitive to only ν_e , clearly showed a deficit.

Table 17.1 also summarizes the results for the ratio of the solar neutrino data to the results predicted from the Monte Carlo simulations (mainly based on SSM) (column 5). It may be clearly observed that for the charged current reactions (only ν_e induced), there is a deficit observed by many detectors like Kamiokande, SAGE, GALLEX, SNO, etc. In future, there are plans to detect solar neutrinos by using even larger detectors, as well as detectors having greater sensitivity.

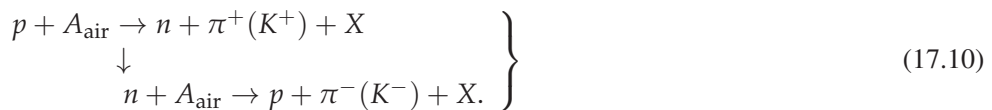
Table 17.1 Solar neutrino detectors and their main characteristics. LS stands for liquid scintillator detectors.

Experiment	Reaction	Active mass (ton) & detector	E_{th} (MeV)	Data/MC	Location	Period
Homestake	$\nu_e {}^{37}_{17}\text{Cl} \rightarrow {}^{37}_{18}\text{Ar } e^-$	615 C_2Cl_4	0.814	0.32 ± 0.05	Homestake Gold Mine, South Dakota, USA	1967–1994
Kamiokande II III	$\nu_e e^- \rightarrow \nu_e e^-$ $\nu_e e^- \rightarrow \nu_e e^-$	3000 H_2O	9.3/7.5 /7.0	$0.44 \pm 0.13 \pm 0.08$	Mozumi Mine, Japan	1986–90 1990–95
SAGE	$\nu_e {}^{71}_{31}\text{Ga} \rightarrow {}^{71}_{32}\text{Ge } e^-$	50 molten metal, Ga	0.233	0.52 ± 0.03	Baksan Neutrino Observatory, Russia.	1990–2007
GALLEX	$\nu_e {}^{71}_{31}\text{Ga} \rightarrow {}^{71}_{32}\text{Ge } e^-$	30 $\text{GaCl}_3\text{--HCl}$	0.233	0.52 ± 0.03	Gran Sasso Laboratory, Italy.	1991–1997
GNO	$\nu_e {}^{71}_{31}\text{Ga} \rightarrow {}^{71}_{32}\text{Ge } e^-$	30 $\text{GaCl}_3\text{--HCl}$	0.233	0.52 ± 0.03	Gran Sasso Laboratory, Italy.	1998–2003
Super-K I II III IV	$\nu_e e^- \rightarrow \nu_e e^-$	50000 H_2O	4.5 6.5 4.5 3.5	0.42 ± 0.06	Under Mount Ikeno, Japan.	1996–2001 2003–2005 2006–2008 2008–Present
SNO	$\nu_e D \rightarrow e^- p p$ $\nu_x D \rightarrow \nu_x p n$ $\nu_x e^- \rightarrow \nu_x e^-$	1000 pure D_2O	6.75/5/6	0.36 ± 0.06 $.30 \pm .04$ 0.94 ± 0.14	Creighton mine, Sudbury, Canada	1999–2006
Borexino I II	$\nu_x e^- \rightarrow \nu_x e^-$	300 C_9H_{12}	0.250	0.43 ± 0.10	Gran Sasso, Italy	2007–2010 2011–Present
SNO+	$\nu_x e^- \rightarrow \nu_x e^-$ $\bar{\nu}_e p \rightarrow e^+ n$	780 LS	1.0	-	Creighton Mine, Sudbury, Canada	Future
JUNO	$\bar{\nu}_e p \rightarrow e^+ n$	20000 LS	1.0	-	Kaiping South China	Future
Hyper-K	$\nu_e e^- \rightarrow \nu_e e^-$	10^9 liter Water	~ 2.0	-	Kamioa, Japan	Future

17.3 Atmospheric Neutrinos

17.3.1 Introduction

Atmospheric neutrinos are typically produced in the interaction of primary cosmic ray particles with the earth's atmosphere. Cosmic rays are high energy particles, mainly protons and alpha particles, also categorized as primary cosmic rays. The observed energy and isotropy of the cosmic rays suggest that they come from outside the solar system, but within our galaxy, apart from a small component coming from solar flares. There is also a small fraction of cosmic rays that have other galactic and extra galactic sources. The exact source of cosmic rays is not yet known but may possibly be black holes, neutron stars, pulsars, quasars, or even the Big Bang. The composition of the primary cosmic rays are protons (90.6%), alpha particles (9%), and a small fraction of CNO nuclei (0.4%) above ~ 100 MeV/nucleus, and 95.2% protons, 4.5% alpha particles, and 0.3% of CNO nuclei above ~ 2 GeV/nucleus. When these primary cosmic rays interact with the earth's atmosphere, they produce secondary cosmic rays, consisting mainly of pions and kaons:



The cosmic ray spectrum starts from the sub-GeV energy region and extends roughly up to 10^{11} GeV [886]. In Figure 17.6, typical cosmic ray spectra for the proton and the alpha particles have been shown. When primary cosmic rays enter into the top of the earth's atmosphere,

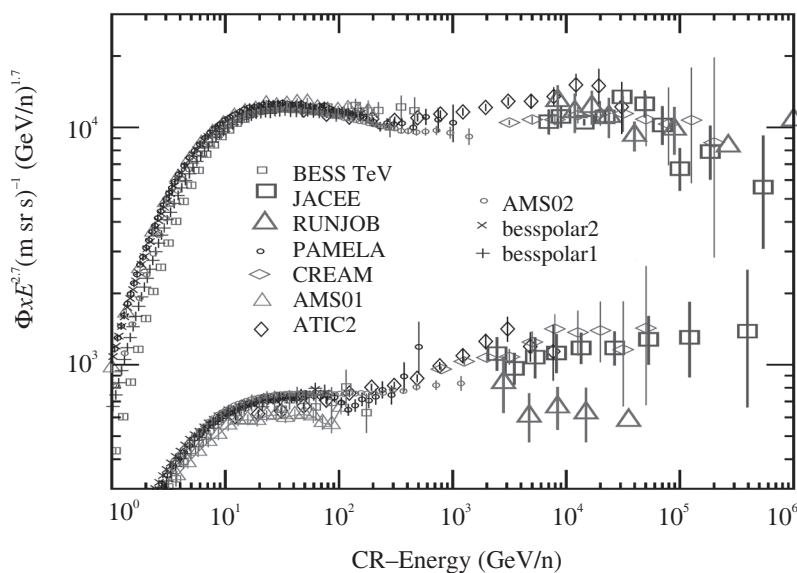


Figure 17.6 Primary cosmic ray flux for the proton (top line with experimental points) and alpha particles (bottom line with experimental points) [887, 888, 889, 890, 891, 892, 893, 117].

they propagate up to an atmospheric depth of about 15 km and produce secondaries through interaction. Subsequently, new particles are produced and gradually, the energy decreases. The energy of the charged particles is gradually absorbed by ionizing the matter present in the earth's atmosphere, as they pass through it.

The earth's geomagnetic field plays a very important role in the modulation of the intensity of cosmic rays. Suppose that the geomagnetic effect of the earth's magnetic field is switched off. Then the primary cosmic ray flux will almost be isotropic. However, the earth's geomagnetic field affects the cosmic rays, both outside, as well as inside the earth's atmosphere (Figure 17.7). Outside the atmosphere, it does not allow low energy particles to come in. Inside the atmosphere, it bends the charged secondaries. Of course, this depends upon the point of interaction, the direction and radius of curvature of the cosmic rays. Particularly, it is the strength of the horizontal component of the geomagnetic field (B_h) which plays a decisive role in the modulation of the cosmic ray flux. In literature, this is known as the effect due to rigidity cut off. The number of cosmic muons depend considerably on B_h . For example, at the INO site (Theni $9^{\circ}96'7''$, $77^{\circ}26'7''$ in India), this strength is ~ 40000 nT, while at the Super-K (Kamioka mine $36^{\circ}26''$, $137^{\circ}10''$ in Japan), it is ~ 30000 nT and at the South Pole ($-90^{\circ}, 0^{\circ}$), the strength is ~ 16000 nT. Therefore, the maximum effect would be at the INO site and the minimum at the South Pole site. In fact, the east–west effect is a well-established phenomenon, where it was observed that the cosmic ray intensity is, in fact, greater in the west than in the east, showing that most of the primary cosmic ray particles are positively charged. The effect of the geomagnetic field in turn results in bending of the μ^+ beam, which enhances the east–west effect, while the μ^- bending tends to cancel east–west effect.

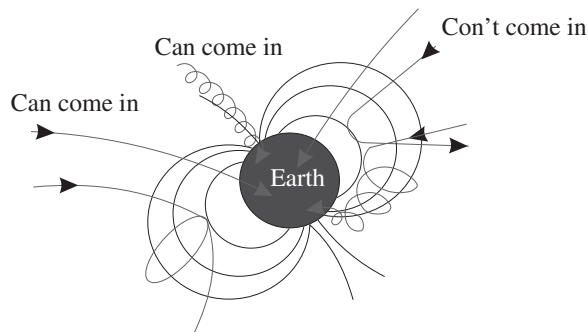


Figure 17.7 Rigidity cut off [894].

Since atmospheric neutrinos are created through the hadronic interactions of the primary cosmic rays and the nuclei present in the atmosphere, the number of produced pions and kaons which give rise to neutrinos depend more on the number of nucleons than the total number of nuclei, implying a larger contribution of atmospheric neutrinos from a heavier nucleus than the proton. For example, α particles carry $\sim 15\%$ and CNO nuclei $\sim 3.6\%$ above ~ 2 GeV/nucleon, of the total nucleons in the cosmic rays despite 4.5% alpha particles and 0.3% of CNO nuclei being present in the cosmic rays.

The differential energy spectrum follows a power law of the form:

$$N(E)dE \propto E^{-\gamma}dE \quad (17.11)$$

with features known as “knee” and “ankle” at $2 - 5 \times 10^{15}$ eV and $2 - 8 \times 10^{18}$ eV, respectively. Hence, the spectrum steepens to $\gamma \simeq 3$ at the ‘knee’. At the ‘ankle’, there is a flattening of spectrum, again resulting in $\gamma \simeq 2.7$. This has been shown in Figure 17.8.

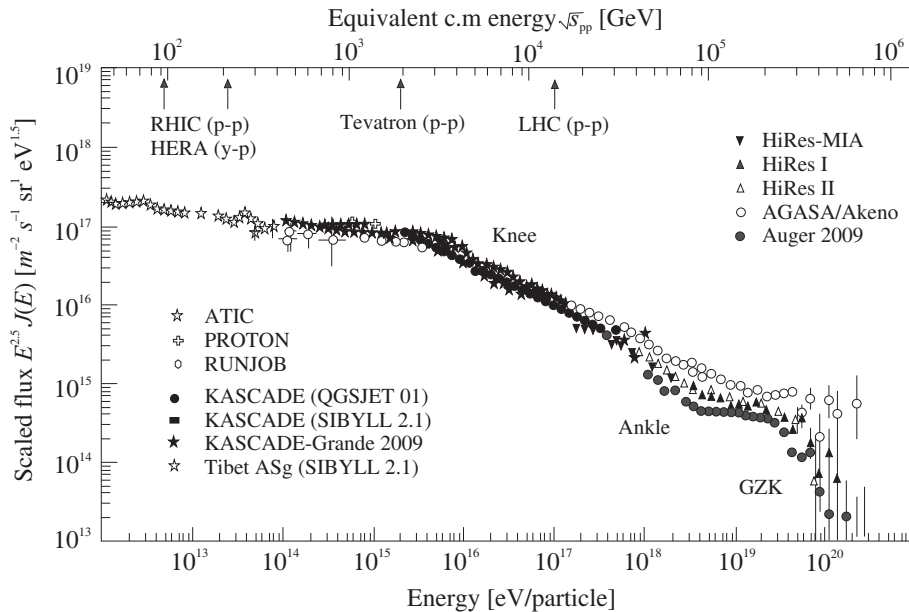
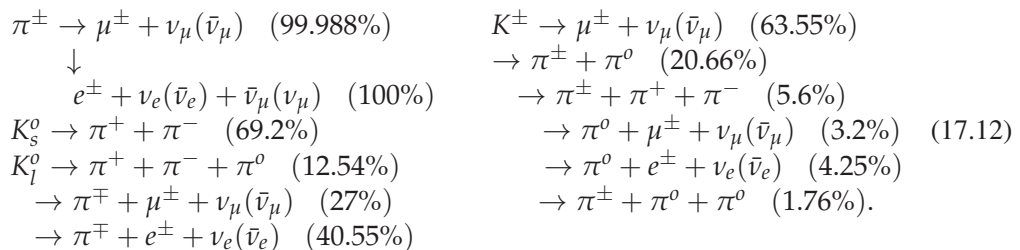


Figure 17.8 Primary cosmic ray flux for the proton showing knee, ankle, and GZK region [117].

The produced muon (μ^+) is also unstable and decays to a positron (e^+), a $\bar{\nu}_\mu$, and a ν_e (Figure 17.9). This decay chain is represented as:



The sources of neutrinos of energies up to around 100 GeV are mainly pion decays, while the higher energy neutrinos are produced from kaon decays, as the mean free path for the pions becomes sufficiently large at higher energies and they are able to reach the earth before decaying into muons and neutrinos (Figure 17.10). The most abundant charged particles at sea level are muons, which are produced high in the atmosphere (~ 15 km) and come to ground,

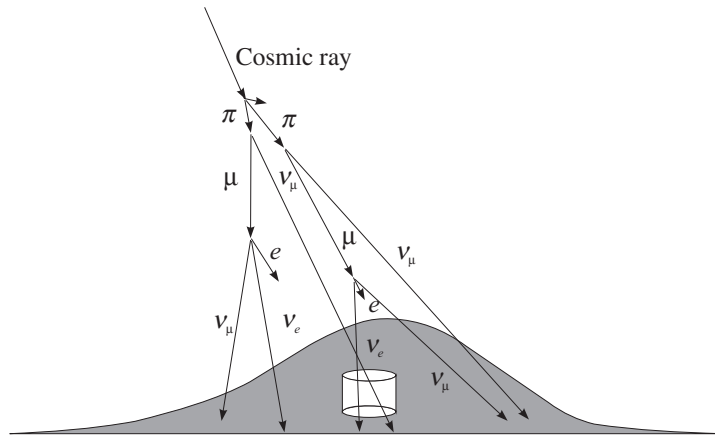


Figure 17.9 Schematic diagram of the production of atmospheric neutrinos.

after ionization losses. The number of μ^+ is more than the number of μ^- , because there are more π^+ , K^+ than π^- , K^- , as there are more protons than neutrons present in the primary cosmic ray components. In general, with the increase in the energy of the muons, the ratio of μ^+ to μ^- increases, due to increase in the number of K^+ . This is because a large number of K^- are absorbed by protons through strong interactions while there is no absorption of K^+ due to the conservation of strangeness.

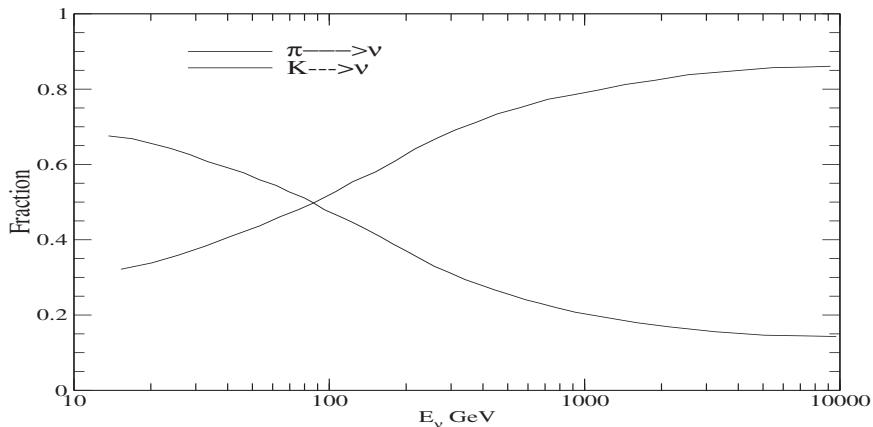


Figure 17.10 Fractional contribution of pions and kaons to the flux of neutrinos for the vertical direction.

The atmospheric neutrino flux is a convolution of the primary spectrum at the top of the atmosphere with a yield (Y) of neutrinos per primary particle. The flux of the neutrinos of type i can be represented as:

$$\Phi_{\nu_i} = \Phi_p \otimes R_p \otimes Y_{p \rightarrow \nu_i} + \sum_A \{ \Phi_A \otimes R_A \otimes Y_{A \rightarrow \nu_i} \}, \quad (17.13)$$

where $\Phi_{p(A)}$ is the flux of the primary protons (nuclei of mass number A) outside the influence of the geomagnetic field and $R_{p(A)}$ represents the filtering effect of the geomagnetic field.

In the pion decays at rest (Chapter 6), the energy carried by the neutrinos is given by:

$$E_{\nu_\mu(\bar{\nu}_\mu)} = \frac{m_\pi^2 - m_\mu^2}{2m_\pi} \sim 30 \text{ MeV},$$

and the muons carry the rest of the energy. When a muon decays, each particle in the final state ($e^\pm + \nu_e(\bar{\nu}_e) + \bar{\nu}_\mu(\nu_\mu)$) carries almost one-third of the muon's energy, that is, approximately 36.5 MeV. When the pions are in flight, then also the energy distribution of the decay products of muons holds approximately the same distribution. Therefore, for all types of the pion spectrum, the flux ratio of the neutrinos from Eq. (17.12) for $\Phi(\nu_\mu + \bar{\nu}_\mu)$ to $\Phi(\nu_e + \bar{\nu}_e)$ is expected to be in the ratio 2:1. Moreover, the ratio of $\Phi(\nu_\mu)$ to $\Phi(\bar{\nu}_\mu)$ is expected to be ~ 1 , because π^+ and π^- decay to ν_μ and $\bar{\nu}_\mu$, respectively. Moreover, inspecting Eq. (17.12) indicates that the $\Phi(\nu_e)$ to $\Phi(\bar{\nu}_e)$ ratio should also be equal to the $\Phi(\pi^+)$ to $\Phi(\pi^-)$ ratio. In the experiments, the atmospheric muon ratio $\Phi(\mu^+)$ to $\Phi(\mu^-)$ is observed with a reasonably good precision using the $\Phi(\pi^+)$ to $\Phi(\pi^-)$ ratio, which in turn gives the ratio of $\Phi(\nu_e)$ to $\Phi(\bar{\nu}_e)$ and $\Phi(\nu_\mu)$ to $\Phi(\bar{\nu}_\mu)$ with a good precision. Figure 17.11 shows the μ^+ and μ^- fluxes as a function of the muon momentum at the INO, the Super-K, and the South Pole by integrating over all the zenith and azimuthal bins for two different heights from the sea level, as well as at the sea level. It may be observed that the geomagnetic field has a strong effect which is described in terms of the rigidity cut off; the flux is maximum at the South Pole site and minimum at the INO site. Moreover, the number of muons decreases considerably at the sea level as compared to a height of say 8 km above the sea level.

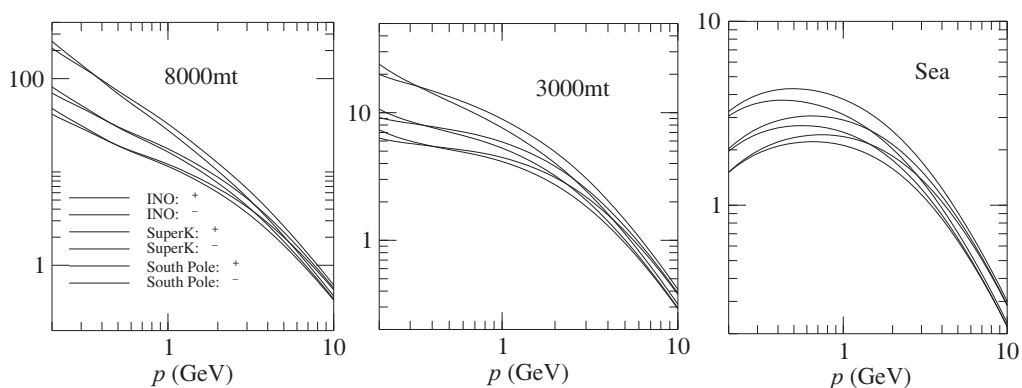


Figure 17.11 μ^+ (solid line) and μ^- (dashed line) fluxes as a function of the muon momentum at the INO, Super-K and South Pole by integrating over all the zenith and azimuthal bins for the two different heights from the sea level, as well as at the sea level.

In Figure 17.12, we show one year average of the atmospheric neutrino fluxes at the SK site ($36^\circ 26''$, $137^\circ 10''$), the INO site ($9^\circ 59''$, $77^\circ 16''$), the South Pole ($-90^\circ 00''$, $0^\circ 00''$), and the Pyhäsalmi ($63^\circ 40''$, $6^\circ 41''$) mine (Finland), averaging over all the directions [897]. The qualitative features are same at all the sites. However, we find a difference of flux among the

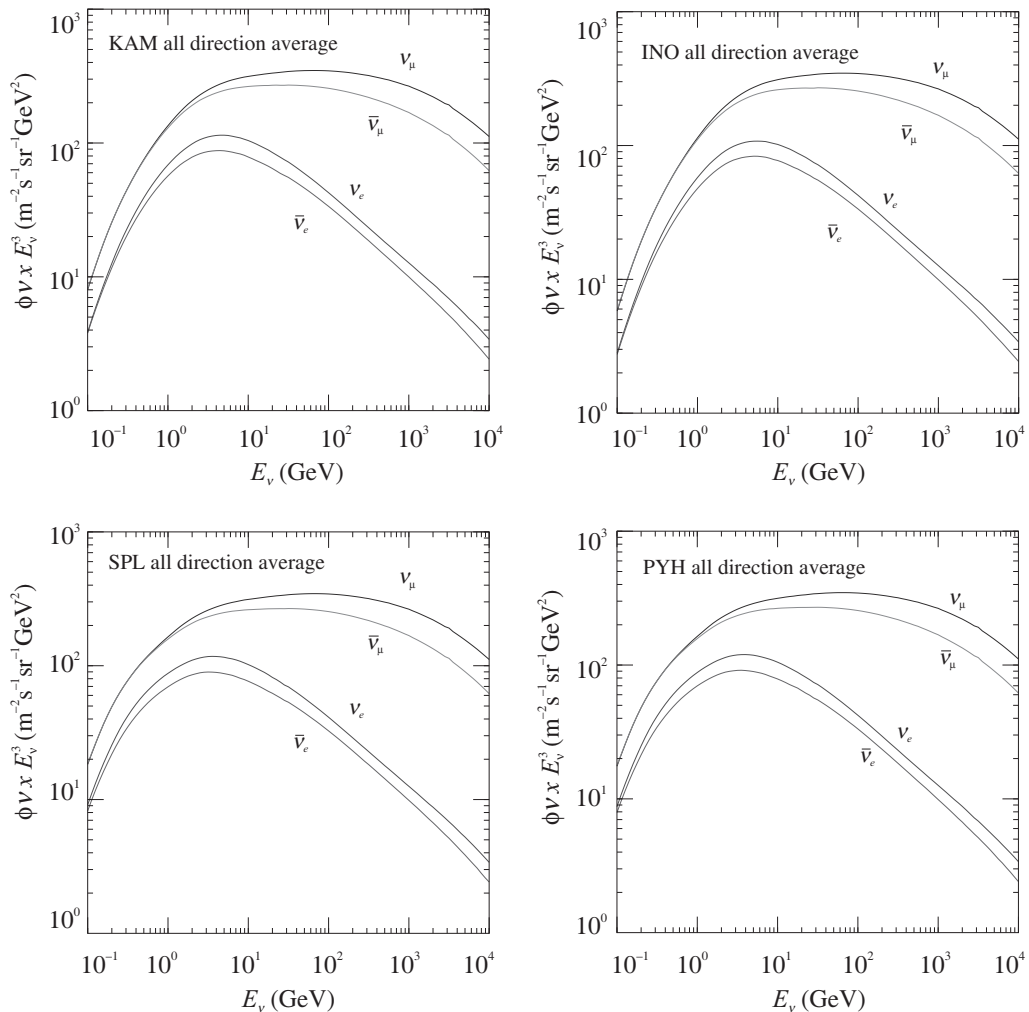


Figure 17.12 All-direction averaged atmospheric neutrino flux for four sites averaging over one year. KAM stands for the SK site, INO for the INO site, SPL for the South Pole, and PYH for the Pyhäsalmi mine [897].

sites by a factor ~ 3 , at the low energy end, due to the large difference in the cut off rigidity among these sites. The differences of the flux among the sites above 10 GeV is small as shown in the figure.

17.3.2 Detection

The pioneering experiments to observe atmospheric neutrinos were started in the mid-1960s. These experiments were carried out in the Kolar Gold Field mines in India [895] and the East Rand Proprietary mine in South Africa [896]. These experiments were carried out in extremely deep underground laboratories at the depth of about 8000 meters water equivalent; the neutrino interactions occurring in the surrounding rocks were observed. At such depth, it was expected

that the charged particles traversing the detectors almost horizontally would be of atmospheric neutrino origin. Most of the observed events were attributed to charged current interactions originating due to the interaction of muon type neutrinos, since it was required that the particle should penetrate through the rock as well as the detector.

The next generation of atmospheric neutrino experiments [898, 899, 900, 901, 902, 903] began in the mid-1980s in Europe (NUSEX and Frejus detectors), USA (IMB-3 detector), and Japan (Kamiokande detector). The main aim of these experiments was to look for nucleon decay candidates to verify the predictions of the grand unified theories (GUTs). In these experiments, the most serious background for proton decay was the events generated by atmospheric neutrinos. Therefore, the first requirement of these experiments was to study the atmospheric neutrino events in order to understand the proton decay background. Kamiokande measured the number of single Cherenkov ring e -like and μ -like events, which were mostly due to the charged current interactions of ν_e and ν_μ , respectively. One of the important observations made in 1988 was that the number of μ -like events had a significant deficit compared with the Monte Carlo prediction, while the number of e -like events were in agreement to the Monte Carlo predictions. This is known as the atmospheric neutrino anomaly. Kamiokande's results were later verified by the IMB water Cherenkov experiment in 1991 and in the updated analysis of the Kamiokande experiment in 1992, as well as in the Soudan-2 experiment in 1997.

Although not very conclusive, during the mid-1990s, the Kamiokande experiment found that the μ -like events show a deficit which was dependent on the zenith angle, and therefore on the neutrino flight length. The zenith angle distributions were studied for the multi-GeV fully contained events, as well as for the partially contained events. Fully contained events are those where the neutrino interacts within the volume of the inner detector, and no particle escapes the detector, while partially contained events are those where one or more particles penetrate far enough to leave the detector, and hence, their energy cannot be reliably measured. For example, higher energy charged current interactions may result in the muon exiting the detector. The vertically downward going neutrinos travel about 15 km, while the vertically upward going neutrinos travel about 12800 km (the earth's diameter) before interacting with the detector. The asymmetry in the downward going neutrinos vs. the upward going neutrinos was observed in 1996, in the Super-Kamiokande experiment, with a 50 kT water Cherenkov detector, where the data clearly showed the deficit of the upward going events in the multi-GeV energy range. Moreover, a smaller μ -like/ e -like event ratio than the predictions of the Monte Carlo were model also observed. Similar observations were made by the MACRO and the Soudan-2 experiments.

Presently, there are five experiments, viz., the Super-Kamiokande, the MINOS, the SNO, the IceCube, and the ANTARES, which are sensitive to atmospheric neutrinos; many new experiments are being planned for the future. Some important features of these experiments are summarized in Table 17.2.

Table 17.2 Atmospheric neutrino detectors.

Experiment	Reaction	Active mass (ton) & detector	E_{th} (MeV)	Data/MC	Location	Period
Frejus	$p(X, Y)n\pi$ $\pi \rightarrow \mu + \nu_\mu$ $\mu \rightarrow e + \nu_\mu + \nu_e$	900 plastic flash tube	3.5×10^3	$1.06^{+0.19}_{-0.16} \pm 0.15$	Frejus highway tunnel, France	1984– 1988
IceCube	$\nu_l N \rightarrow \nu_l$ +Cascade $\nu_l N \rightarrow l^-$ +Cascade	0.66×10^9 Antarctic Ice	$\approx 10^3$		South Pole, Antarctica	2011– Present
IMB-3	$\nu_\mu \rightarrow \nu_\tau$	8000 Water Cherenkov	15.0	$0.54 \pm 0.005 \pm 0.12$	Morton Salt Mine, Ohio, USA	1982– 1991
Kamiokande	$\nu_e e^- \rightarrow \nu_e e^-$	3000 H ₂ O	7.5	$0.44 \pm 0.03 \pm 0.08$	Mozumi Mine, Japan	1986– 1995
MACRO	$0\nu\beta\beta$	5300 CAL			Gran Sasso, Italy	1995– 2000
MINOS	$\nu_\mu + \text{nucleus}$ $\rightarrow \mu^- + X$	5400 CAL	500		Illinois & Minnesota, USA	2005– 2012
NUSEX		150 ICAL	~ 250	$0.99 + 0.035 - 0.25$	Mont Blanc tunnel, Europe	1982– 1988
Soudan-2		963 ICAL	< 500	$0.55^{+0.27}_{-0.19}$	Soudan Mine, USA	1989– 2001
Super-K I II III IV	$\nu_e e^- \rightarrow \nu_e e^-$ $\nu_e n \rightarrow e^- p$ $\nu_e p \rightarrow e^+ n$	50000 H ₂ O	SubGeV $< 1.3\text{GeV}$ MultiGeV $> 1.3\text{GeV}$	0.42 ± 0.06	Under Mount Ikeno, Japan.	1996–2001 2003–2005 2006–2008 2008–present
JUNO	$\bar{\nu}_e p \rightarrow e^+ n$	20000 LS	1.0	-	Kaiping, China	Future
Hyper-K	$\nu_e e^- \rightarrow \nu_e e^-$	10^9 liter Water	~ 2.0	-	Kamioa, Japan	Future
DUNE	$\nu_e(^{40}\text{Ar}, ^{40}\text{K}^*)e^-$	68000 LAr-TPC	4.5	-	Homestake Mine, USA	Future
INO		50000 ICAL	< 1.0	-	Tamil Nadu, India	Future
PINGU	$\nu_l N \rightarrow \nu_l$ +Cascade $\nu_l N \rightarrow l^-$ +Cascade	6×10^6 Ice	$< 10^4$	-	South Pole, Antarctica	Future

17.4 Reactor Antineutrinos

The antineutrino was detected for the first time in 1956 by Reines and Cowan, at Savannah nuclear reactor power plant; since then, reactor antineutrinos have played an important role in both the discovery, as well as in the precision measurements of some of the neutrino oscillation parameters. The isotopes rich in neutrons like ^{235}U , ^{238}U , ^{239}Pu , ^{241}Pu , through the fission processes in the power reactors, undergo a series of decays which may be broadly represented by the reaction:



which produce approximately six antineutrinos per fission. The mixture of the isotopes produced is complex (mixture of several isotopes), which results into a continuous energy spectrum of $\bar{\nu}_e$ s, with energies ranging between 0-8 MeV and the average energy around 2-3 MeV, along with the emission of $\sim 200\text{MeV}$ of fission energy. The flux of the antineutrinos (Fig. 17.13) is proportional to the thermal power of the reactors core. For example, the fission

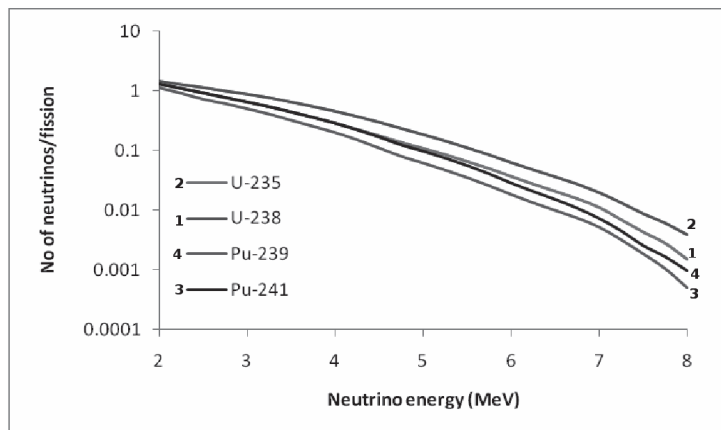
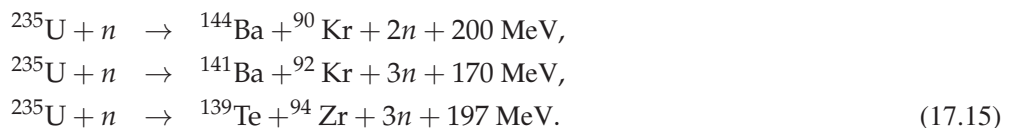


Figure 17.13 Typical antineutrino spectra [904].

reaction in ^{235}U produces fission products such as Ba, Kr, Sr, Cs, I, and Xe having atomic masses in the intermediate mass range, viz., 95 and 145:



Typically, if in one fission reaction, 200 MeV of energy is released which corresponds to $3.2 \times 10^{-11}\text{J}$ of energy; on an average, if six $\bar{\nu}_e$ s are released, then for a Giga-Watt reactor, there would be typically 2×10^{20} $\bar{\nu}_e$ s being produced in each second corresponding to a flux density given by:

$$\Phi(\bar{\nu}_e) \sim 1.6 \times 10^{19} \frac{P/\text{GW}}{L^2/\text{m}^2} \text{m}^{-2}\text{s}^{-1}, \quad (17.16)$$

where P is thermal power in Giga-Watt (GW) and L is the distance in meters from the reactor. In Figure 17.13, we have shown typical antineutrino spectra emitted by various sources.

Instead of fission rates, generally, fission fractions in the core simulation are used, which is the ratio of the fission rate of an isotope over the total rate. The reactor antineutrino spectrum is calculated as:

$$\Phi(E_\nu) = \frac{W_{\text{th}}}{\sum_i f_i e_i} \cdot \sum_i f_i \cdot S_i(E_\nu), \quad (17.17)$$

where E_ν is the antineutrino energy, and f_i , e_i , and $S_i(E_\nu)$ are the fission fraction, thermal energy released in each fission, and the antineutrino spectrum per fission for the i th isotope, respectively.

17.4.1 Detection

The inverse beta decay (IBD) reaction, $\bar{\nu}_e + p \rightarrow e^+ + n$ with liquid scintillators (LS) rich in hydrogen, is the classical channel to detect reactor antineutrinos. After thermalization, the neutron is captured by hydrogen or other nuclei (e.g., Gd, Cd, Li) and a delayed signal, tens or hundreds microseconds behind the prompt signal (Figure 1.8) is created. The reactor antineutrino experiments, which were performed during the 1970s and 1980s, initiated efforts to have a better knowledge of the flux coming out from the reactor's core. The modern day antineutrino reactor experiments started with CHOOZ [905] and Palo Verde [906] reactor experiments. The CHOOZ operated in 1997–1998 in France and Palo Verde, in 1998–2000, in USA. CHOOZ used two 4.2 GW reactors and scintillator detectors filled with 0.1% Gd placed 998 m and 1115 m away, while Palo Verde used three reactors of total capacity 11.6 GW and detectors at distances of 750, 890 and 890 m from the three reactors. The current reactor neutrino experiments like Daya Bay, Double Chooz and RENO have led neutrino physics into the precision era. The characteristics of several detectors have been listed in Table 17.3 and Table 17.4, for the short baseline and long baseline experiments, respectively.

A multi-purpose detector, the KamLAND, is placed at the site of the former Kamiokande experiment with a vertical overburden of 2,700 meters water equivalent (m.w.e.), with the primary goal to search for reactor antineutrino ($\bar{\nu}_e$) oscillations. It is surrounded by 55 Japanese nuclear reactor cores. The $\bar{\nu}_e$ flux weighted average baseline is 180 km. The KamLAND consists of 1 kton of ultrapure liquid scintillator. The JUNO, near Guangzhou in South China, is a next generation experiment. A total power of 26.6 GW will be available by 2020, when JUNO is scheduled to start taking data.

Table 17.3 Reactor (short baseline) neutrino detectors.

Experiment	Reaction	Active mass (ton) & detector	E_{th} (MeV)	Location	Period
CHOOZ	$\bar{\nu}_e p \rightarrow e^+ n$	5 Gd-LS	1.8	Ardenne, France	1997–1998
Gösgen	$\bar{\nu}_e p \rightarrow e^+ n$	377 liter LS	1.8	Gösgen Switzerland	1985–
Double CHOOZ	$\bar{\nu}_e p \rightarrow e^+ n$	10.16 Gd-LS	1.8	Ardenne, France	2010–2015
Nucifer	$\bar{\nu}_e p \rightarrow e^+ n$	850 liter Gd-LS	1.8	CEA-Saclay, France	2012
NEOS	$\bar{\nu}_e p \rightarrow e^+ n$	~ 1 Gd-LS	1.8	Younggwang, Korea	2015–2016
Neutrino-4	$\bar{\nu}_e p \rightarrow e^+ n$	$1.8 m^3$ volume Gd-LS	~ 1.8	Dimitrovgrad, Russia.	2016–Present
STEREO	$\bar{\nu}_e p \rightarrow e^+ n$	Gd-LS	~ 2.0	Grenoble, France	2016–Present
RENO	$\bar{\nu}_e p \rightarrow e^+ n$	16 Gd-LS	1.8	Younggwang, Korea	2011–Present

Table 17.4 Reactor (long baseline) neutrino detectors.

Experiment	Reaction	Active mass (ton) & detector	E_{th} Energy (MeV)	Location	Period
Palo Verde	$\bar{\nu}_e p \rightarrow e^+ n$	11.34 GD-LS	0.04 (low) 0.6 (high)	Arizona, USA	1998–2000
KamLAND	$\bar{\nu}_e p \rightarrow e^+ n$	~ 1000 Water	~ 1.8	Kamioka, Japan	2002–Present
Daya Bay	$\bar{\nu}_e p \rightarrow e^+ n$	20 (GD-LS) +20 (LS) +37 (oil)	~ 1.8	Southern coast of China	2011–Present
RENO-50	$\bar{\nu}_e p \rightarrow e^+ n$	18000 LS	~ 1.8	Younggwang, Korea	Future
JUNO	$\bar{\nu}_e p \rightarrow e^+ n$	20000 LS	1.0	Kaiping South China.	Future

17.5 Supernova Neutrinos

17.5.1 Introduction

Supernova neutrinos and antineutrinos of all flavors are associated with one of the most explosive and violent astrophysical events: the supernova explosion, which occurs during the

death phase of a massive star ($M_{\text{Star}} \gtrsim 8M_{\odot}$). Such massive stars become unstable at the end of their lives. They collapse and eject their outer mantle through a supernova explosion. These supernova explosions are the sources of the most powerful cosmic neutrinos in the MeV range. Colgate and White [907] and independently Arnett [908], were among the first who pointed out the importance of neutrinos in the context of stellar core collapse and theorized the mechanism through which massive stars die in a supernova (SN) explosion. The huge amount of energy released in a supernova explosion is due to the difference in the gravitational binding energy of a star and a neutron star:

$$\begin{aligned} E_{BE} &\approx \left(-\frac{3}{5} \frac{GM_S^2}{R_S} \right) - \left(-\frac{3}{5} \frac{GM_{NS}^2}{R_{NS}} \right) \text{ and } R_S \gg R_{NS} \\ &\approx 3.6 \times 10^{47} \left(\frac{M_{NS}}{1.5 M_{\odot}} \right)^2 \left(\frac{R_{NS}}{10 \text{ km}} \right)^{-1} \text{ J,} \end{aligned} \quad (17.18)$$

where M_S and R_S are the mass and radius of a star which can undergo supernova explosion, M_{\odot} is mass of the sun, M_{NS} and R_{NS} are, respectively, the mass and the radius of a neutron star. During such an event, the exploding star becomes comparable in brightness to its entire host galaxy! In course, colossal amounts of energy is released, equal to the total amount of energy that the sun radiates in 10 million years. The supernovae arise from two different final stages of stars. They are either caused by the thermonuclear explosions of a white dwarf within a binary system or by the core collapse of massive stars. They are in general classified as type I and type II supernovae. The type I supernovae occur in binary systems; a binary system is a system of two stars orbiting one another, and among them, one of the stars is a white dwarf, while the other can be a giant star or an even smaller white dwarf. Type I supernovae are further divided into subclasses, for example, type Ia, Ib, Ic according to the existence of hydrogen, helium, or silicon spectral lines. We shall discuss the formation and death of stars in Chapter 19, where the supernova explosion mechanism will also be explored.

In a supernova explosion, most of the gravitational energy released in the core collapse is carried by neutrinos. Such neutrino bursts carry $\approx 3.6 \times 10^{47}$ J of energy in a very short period of time [909]. It is considered that these neutrinos could provide valuable information about the proto-neutron star core, its equation of state, core collapse, and supernova explosion mechanism; they can help to have a better understanding of supernova physics [909, 910]. After the observation of supernova neutrinos from SN1987A at Kamiokande, IMB, and BAKSAN [911, 912], the feasibility of detecting such events in the future has now been given serious consideration. For example, experiments like the Super-K [913], LVD [914], AMANDA [915], BOREXino [916], OMNIS [917], LAND [918], HALO [919], ICARUS [920], etc. are in various stages of operation while SNO+ [921], Hyper-K [922] experiments are being developed. Experiments like DUNE [629] and JUNO [923, 924] have been planned to study the physics related to supernova neutrinos in the near future. A list of the present and future experiments, having sensitivity to supernova neutrinos/antineutrinos is given in Table 17.5. These experiments are planned to use detectors with various nuclei as the target materials.

The supernova neutrino/antineutrino fluxes are determined from numerical simulations of the core collapse supernova explosion of a star and depend on the initial properties of the

Table 17.5 Supernova neutrino detectors.

Experiment	Reaction	Active mass (ton) & detector	E_{th} (MeV)	Location	Period
Baikal		Cherenkov	10^4	Lake Baikal, Russia	1980– 1998
IMB	$\nu_\mu \rightarrow \nu_\tau$	8000 Water Cherenkov	15.0	Morton Salt Mine, Ohio, USA	1982– 1991
Kamiokande	$\nu_e e^- \rightarrow \nu_e e^-$	3000 H_2O	7.5	Mozumi Mine, Japan.	1986– 1995
LSD	$\bar{\nu}_e p \rightarrow e^+ n$	90 LS	5	Mont Blanc Laboratory	1984– 1999
LVD	$\bar{\nu}_e p \rightarrow e^+ n$	1800 LS	0.5,4.0	Gran Sasso, Italy	1992– 2016
ICARUS	$\nu_e(^{40}\text{Ar}, ^{40}\text{K})e^-$	600 LAr	~ 5	Gran Sasso, Italy	Future
KamLAND	$\bar{\nu}_e p \rightarrow e^+ n$	~ 1000	~ 1.8	Kamioka, Japan	2002– Present
MiniBooNE	$\nu_\mu \rightarrow \nu_e$	800 Mineral oil		Fermilab, USA	2002– 2017
HALO	$\nu_e + \text{Pb} \rightarrow e^- + \text{Bi}^*$ $\text{Bi}^* \rightarrow \text{Bi} + \gamma + n$ $\nu_x + \text{Pb} \rightarrow \nu_x + \text{Pb}^*$ $\text{Pb}^* \rightarrow \text{Pb} + \gamma + n$	1000 He & Pb	18	Creighton Mine in Sudbury, Canada	2015– Present
JUNO	$\bar{\nu}_e p \rightarrow e^+ n$	20000 LS	1.0	Kaiping South China.	Future
DUNE	$\nu_e(^{40}\text{Ar}, ^{40}\text{K}^*)e^-$	68000 LAr-TPC	4.5	Homestake Mine, USA.	Future

collapsing star like its mass, density, and equation of state, as well as, on various physical processes controlling the explosion like the initial prompt burst of the neutrinos following the neutronization, accretion, and cooling in the late phases and the neutrino transport in the dense star matter [925, 926, 927, 928]. The neutrino/antineutrino fluxes are found to be sensitive to the luminosities L_ν of the various neutrino/antineutrino flavors, which are believed to be equal for all the six flavors of neutrinos/antineutrinos ν_e , $\bar{\nu}_e$, ν_x , and $\bar{\nu}_x$ ($x = \mu, \tau$), due to the assumption of equipartition of total available energy amongst various flavors. Some recent calculations have also been done assuming luminosities for ν_x different from the luminosities

of $\nu_e(\bar{\nu}_e)$ and varying them in the range of $0.5L_{\nu_e} < L_{\nu_x} < 2L_{\nu_e}$, keeping the luminosities of ν_e and $\bar{\nu}_e$ to be the same [929, 930, 931, 932, 933, 934]. The simulated neutrino/antineutrino fluxes and mean energies of their various flavors are, in general, distinct from each other due to the differences in their interaction with dense star matter, which has an excess of neutrons over protons. This difference leads to ν_e losing more energy as compared to $\bar{\nu}_e$, which loses more energy than ν_x ($x = \mu, \tau$, and their antineutrinos), as $\nu_x(\bar{\nu}_x)$ interacts only through neutral current interaction (due to higher threshold energy for charged current reactions induced by ν_x), while ν_e and $\bar{\nu}_e$ interact through neutral as well as charged current interactions. This gives a hierarchical structure of mean neutrino/antineutrino energies ($\langle E_{\nu(\bar{\nu})} \rangle$) for various flavors, that is, $\langle E_{\nu_e} \rangle < \langle E_{\bar{\nu}_e} \rangle < \langle E_{\nu_x} \rangle$. The various simulations agree on this hierarchical structure of mean neutrino/antineutrino energies, but differ on the actual values which are generally taken to be in the range of $\langle E_{\nu_e} \rangle \approx 10 - 12$ MeV, $\langle E_{\bar{\nu}_e} \rangle \approx 12 - 15$ MeV, and $\langle E_{\nu_x} \rangle \approx 16 - 25$ MeV [929, 930, 931, 932, 933, 934]. However, a lower value of $\langle E_{\nu_e} \rangle$ has also been obtained in some recent studies [935], when additional medium effects were taken into account. These additional medium effects are generated by neutrino–neutrino self interactions [936, 937, 938, 939, 940] and neutrino–matter interactions when primary neutrinos of all the flavors propagate through a medium of very high neutrino and matter densities, causing flavor conversions [941, 942, 943, 944].

The simulated neutrino flavor spectra at the surface of a star are subjected to various uncertainties arising from the uncertainties in the theoretical parameters used in simulation studies of the explosion and propagation of neutrinos inside the dense star matter. This leads to large variations in the predicted spectra for various flavors of neutrino/antineutrino [929, 930] calculated by different authors. Figure 17.14 represents supernova (a) neutrino and (b) antineutrino fluxes simulated by some of the groups working on simulation for example, Totani et al. [925], Duan et al. [937] and Gava et al. [938] for electron neutrinos.

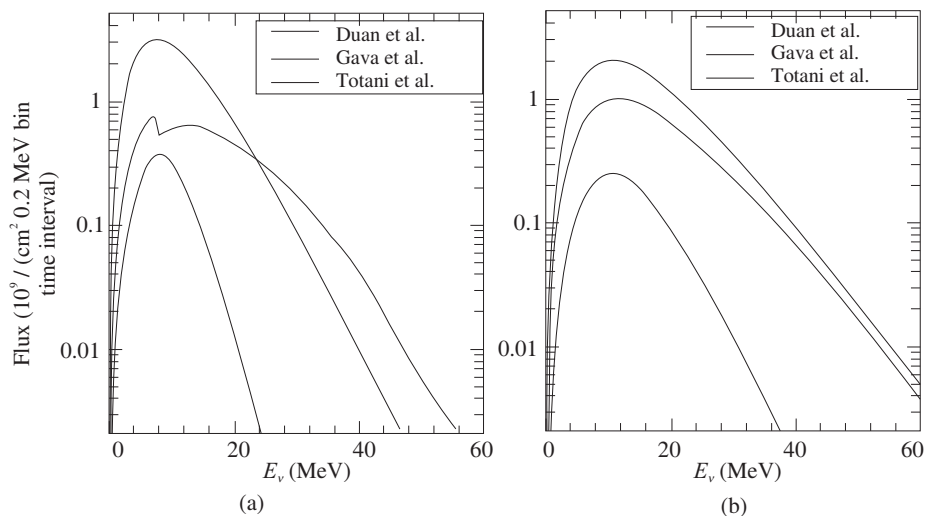


Figure 17.14 Supernova (a) neutrino and (b) antineutrino fluxes simulated by some of the groups like Totani et al. [925] (dashed-dotted line), Duan et al. [937] (solid line) and Gava et al. [938] (dashed line).

17.5.2 Neutrino emission in supernova explosions

Neutrinos are produced during the collapse of the core when electrons are captured by protons and nuclei leading to neutronization of the core; neutrinos are also produced through the process of thermal emission. Some of the several neutronization reactions are:

- Electron capture by nuclei:



- Electron capture by free proton:



Some of the thermal emission processes are:

- Pair annihilation:



- Plasmon decay:



- Photoannihilation:



- Electron–nucleon Bremsstrahlung:



- Nucleon–nucleon Bremsstrahlung:



Each neutrino emission process has an inverse process corresponding to absorption. Both the absorption and the scattering processes delay the free escape of neutrinos from a collapsing core. The most important processes are as follows:

- Free nucleon scattering:



- Coherent scattering by heavy nuclei ($A > 1$):

$$\nu + {}^A_Z X \rightarrow \nu + {}^A_Z X. \quad (17.27)$$

- Nucleon absorption:

$$\nu_e + n \rightarrow e^- + p. \quad (17.28)$$

- Electron–neutrino scattering:

$$e^- + \nu \rightarrow e^- + \nu. \quad (17.29)$$

Similar processes also occur for antineutrinos.

17.5.3 Detection

Many neutrino detectors are connected through the supernova early warning system (SNEWS), which will trigger experiments to record and save additional data if a sudden influx of neutrinos (indicating a supernova) arrives. On February 23, 1987, scientists caught neutrinos from a supernova (SN1987A) in a nearby galaxy, the large magellanic cloud (LMC), 50 kilo parsec away from the earth. The two water Cherenkov detectors, one in Japan, Kamiokande-II, and the other in the United States, the IMB, observed 19 events within 13 seconds, with timing consistent with the optical observation of the SN1987A explosion. Two smaller scintillation detectors, the BAKSAN and LSD also reported several events; however, the evidences were not very conclusive. The observation of neutrinos from SN1987A has been a major event in experimental neutrino physics which has been recognized by awarding the Nobel prize in physics to M. Koshiba, the leader of the Kamiokande experiment in 2002.

17.6 Geoneutrinos

Geoneutrinos are electron antineutrinos released in the decay of radioactive elements; they are distributed throughout the earth's interior. These geoneutrinos are, in fact, the only source of information about the geochemical composition of the earth's core. They are emitted in the decay chain of ${}^{40}\text{K}$, ${}^{232}\text{Th}$, and ${}^{238}\text{U}$:

$${}^{238}\text{U} \rightarrow {}^{206}\text{Pb} + 8 {}^4\text{He} + 8e^- + 6\bar{\nu}_e + 51.7 \text{ MeV}, \quad (17.30)$$

$${}^{235}\text{U} \rightarrow {}^{207}\text{Pb} + 7 {}^4\text{He} + 4e^- + 4\bar{\nu}_e + 46.4 \text{ MeV}, \quad (17.31)$$

$${}^{232}\text{Th} \rightarrow {}^{208}\text{Pb} + 6 {}^4\text{He} + 4e^- + 4\bar{\nu}_e + 42.7 \text{ MeV}, \quad (17.32)$$

$${}^{40}\text{K} \rightarrow {}^{40}\text{Ca} + e^- + \bar{\nu}_e + 1.31 \text{ MeV} \quad (89.3\%), \quad (17.33)$$

$${}^{40}\text{K} + e^- \rightarrow {}^{40}\text{Ar} + \nu_e + 1.505 \text{ MeV} \quad (10.7\%). \quad (17.34)$$

The first direct measurement of the geoneutrino flux was made by the BOREXino and KamLAND collaborations. Only ^{238}U and ^{232}Th chains are measurable with the neutron inverse beta decay process.

The geoneutrino spectrum extends up to ~ 4.5 MeV (Figure 17.15) and the contributions originating from the different elements can be distinguished according to their different endpoints, that is, geoneutrinos with $E > 2.25$ MeV are produced only in the uranium chain. In the future, a few detectors are planned to further study the geoneutrinos, like SNO+, which is filled with 780 tons of liquid scintillator in a 12 m diameter acrylic sphere, shielded by ultra pure water along with 9000 photomultipliers.

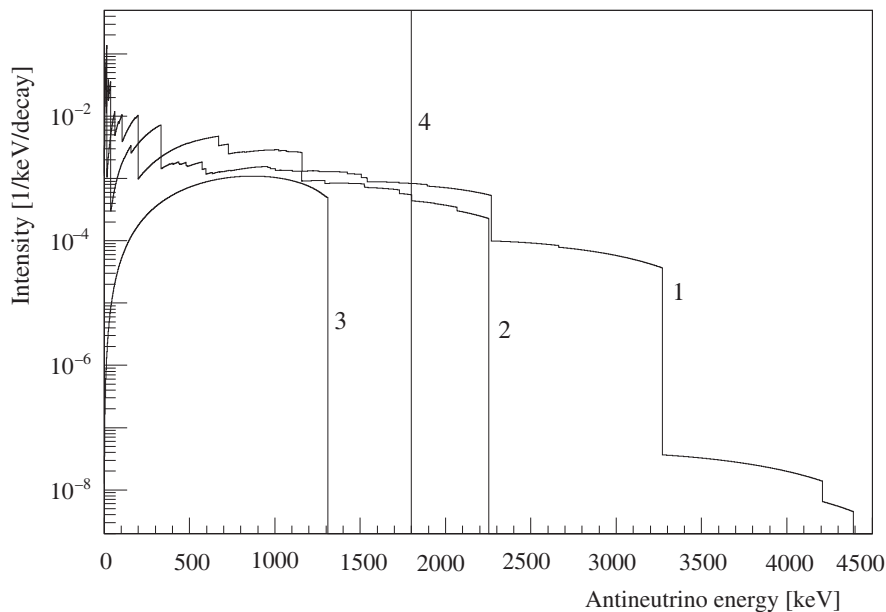


Figure 17.15 $\bar{\nu}_e$ energy distributions for (1) ^{238}U (solid), (2) ^{232}Th (dotted), and (3) ^{40}K (dash-dotted) decay. The vertical line (4) represents the $\bar{\nu}_e$ detection threshold for neutron inverse β decay. [945]

The other planned detectors aimed at measuring geoneutrinos are quite amazing. For example, the Hanohano deep-ocean transportable detector which is planned to be a mobile, sinkable 10 kton liquid scintillation detector, would be carried by a ship and deployed in the deep ocean at some 3 to 5 km depth, near Hawaii. The Daya Bay 2 experiment, is characterized by a very large mass of some 20 kton and is supposed to detect up to 400 geoneutrinos per year. However, due to the presence of nuclear power plants in the close vicinity, the detection of geoneutrinos would be quite challenging. The LENA (Low Energy Neutrino Astronomy) detector consists of a huge 50 kton multidisciplinary liquid scintillation neutrino detector; the detection of geoneutrinos is one of its main scientific goals. Table 17.6 lists some detectors which are sensitive to geoneutrinos.

Table 17.6 Geoneutrino detectors.

Experiment	Reaction	Active mass (ton) & detector	E_{th} (MeV)	Location	Period
KamLAND	$\bar{\nu}_e p \rightarrow e^+ n$	~ 1000 water	~ 1.8	Kamioka, Japan	2002– Present
SNO+	$\nu_x e^- \rightarrow \nu_x e^-$ $\bar{\nu}_e p \rightarrow e^+ n$	780 LS	< 1.0	Creighton Mine, Sudbury, Canada	Future
JUNO	$\bar{\nu}_e p \rightarrow e^+ n$	20000 LS	1.0	Kaiping South China	Future

17.7 Relic Neutrinos

Relic neutrinos are one of the most abundant components of the universe. They are also known as the cosmic neutrino background (CNB). These neutrinos are the relics of the Big Bang, originating from the decoupling of matter through weak interactions when the universe was about one second old and the primordial plasma had a temperature of about 1 MeV ($\simeq 10^{10}$ K). Thus, apart from the 3 K black body electromagnetic radiation known as cosmic microwave background radiation (CMBR), the universe is filled with a sea of relic neutrinos. The average relic electron neutrino number density is around $\langle n \rangle \approx 56/\text{cm}^3$, while that of CMBR is $\langle n_\gamma \rangle \approx 450/\text{cm}^3$. These relic neutrinos have played a crucial role in primordial nucleosynthesis, structure formation, and the evolution of the universe as a whole. They may also provide clues about the mechanism of baryogenesis.

The study of CMBR allow us to see into our universe when it was about 3,80,000 years old, right up until primordial recombination. The direct information about the first few seconds of the universe evolution, principally, can be obtained by the detection of relic neutrinos.

These relic neutrinos were formed with a thermal equilibrium spectra, which for neutrinos (ν) and antineutrinos ($\bar{\nu}$), are given by the Fermi–Dirac distribution (with zero neutrino mass):

$$n_{\nu, \bar{\nu}}(p)dp = \frac{1}{(2\pi\hbar)^3} \frac{4\pi p^2 dp}{\exp(pc/kT) + 1}. \quad (17.35)$$

The theory of primordial nucleosynthesis gives us the relation between the temperatures of relic neutrinos and photons, that is,

$$T_\nu = (4/11)^{1/3} T_\gamma,$$

arising from electron–positron annihilation. Given this relation and the current value of $T_\gamma = 2.725 \pm 0.001$ K, the temperature of relic neutrinos should be $T_\nu \approx 1.945$ K $\simeq 2 \times 10^{-4}$ eV.

The detection of relic neutrinos seems to be hardly possible due to the weak interaction of neutrinos with matter and also due to their low energy ($\approx 10^{-4}\text{eV}$). Several methods have been discussed in literature to look for CNB, but there is not much progress. The most promising suggested detection methodology is through IBD in the process $\nu_e + {}^3\text{H} \rightarrow e^- + {}^3\text{He}$, where the signal will correspond to the peak in the electron spectrum. It has been proposed that such detection is possible in the KATRIN experiment [946, 947].

17.8 Accelerator Neutrinos

Pontecorvo and Schwartz, independently, proposed the idea of performing neutrino experiments with accelerators. They proposed the possibility of an experiment making use of a neutrino beam produced by pion decays at proton accelerators. The first accelerator neutrino experiments were performed by a team led by Lederman, Schwartz, and Stenberger in 1962 at the AGS accelerator, Brookhaven and very soon after this experiment, the neutrino beams at CERN were obtained. The accelerator facilities are used to accelerate the protons to very high energies. These highly energetic protons are smashed into a target; the target can be any material, although it has to be able to withstand very high temperatures. When a proton traveling near the speed of light hits a target, it slows down and the proton's energy is used to produce a jet of hadrons. There are different kinds of particles in this jet; however, the most common are pions and kaons. Neutral pions are not part of story, so we can ignore them; however, the charged pions so produced are unstable and decay essentially into muons and neutrinos. A typical sketch of neutrino beam production from hadrons at an accelerator facility is shown in Figure 17.16. A meson, carrying electric charge, can be collimated using electric and magnetic fields

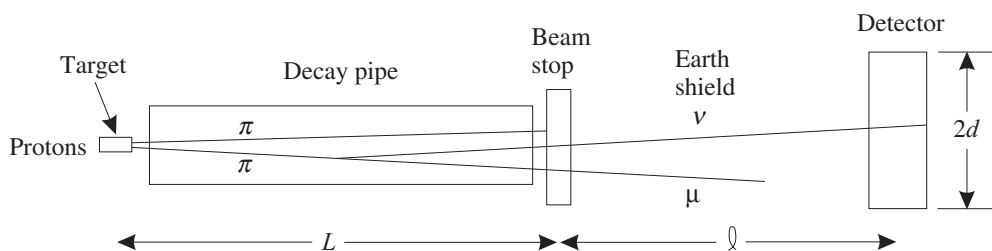


Figure 17.16 Typical sketch of neutrino beam production by accelerators.

known as magnetic horns. Thus, to get a neutrino beam in a certain direction, one points the pion in the direction of the detector. A properly designed horn system can enhance the neutrino flux. To estimate the neutrino flux with better accuracy, it is important to precisely measure the momentum and the angular spectra of the mesons. The probability P of the mesons to decay while traveling a distance L through the decay pipe is given by

$$P = 1 - e^{-\frac{L}{L_0}}, \quad (17.36)$$

where L_0 is the pion decay length and is given by:

$$L_0 = \gamma\beta\tau_{\text{meson}}. \quad (17.37)$$

Here, τ_{meson} is the decay time of the meson and

$$\beta = \frac{|\vec{p}_{\text{meson}}|}{E_{\text{meson}}} \quad \text{and} \quad \gamma = \frac{E_{\text{meson}}}{m_{\text{meson}}}.$$

For example, for a 5 GeV pion, the decay length would be $L_o \sim 280$ m. The energy spectrum of neutrino is obtained using the kinematics of the two-body mesonic decay. Let E_ν and $\cos \theta_\nu$ be, respectively, the energy and angle in the Lab frame and E_ν^{CM} and $\cos \theta_\nu^{\text{CM}}$ be the energy and angle in the CM frame. Then,

$$\begin{aligned} E_\nu &= \gamma (1 + \beta \cos \theta_\nu^{\text{CM}}) E_\nu^{\text{CM}}, \text{ and} \\ \cos \theta &= \frac{\cos \theta_\nu^{\text{CM}} + \beta}{1 + \beta \cos \theta_\nu^{\text{CM}}}, \text{ where} \\ E_\nu^{\text{CM}} &= \frac{m_{\text{meson}}^2 - m_\mu^2}{2m_{\text{meson}}}, \text{ which is 29.8 MeV for } \pi\text{-decay.} \end{aligned} \quad (17.38)$$

The limits on $\cos \theta_\nu^{\text{CM}}$, that is, $-1 \leq \cos \theta_\nu^{\text{CM}} \leq +1$, correspond to the minimum and maximum energies in the Lab frame, that is,

$$\begin{aligned} E_\nu^{\min} &= \frac{E_{\text{meson}}}{m_{\text{meson}}} \frac{m_{\text{meson}}^2 - m_\mu^2}{2m_{\text{meson}}} \left(1 - \frac{|\vec{p}_{\text{meson}}|}{E_{\text{meson}}} \right) \\ &= \frac{m_{\text{meson}}^2 - m_\mu^2}{2(E_{\text{meson}} + |\vec{p}_{\text{meson}}|)} \\ &\simeq \frac{m_{\text{meson}}^2 - m_\mu^2}{4E_{\text{meson}}} \quad (\because E_{\text{meson}} = |\vec{p}_{\text{meson}}|) \\ &\sim 0 \text{ for } E_{\text{meson}}^2 \gg m_{\text{meson}}^2. \\ E_\nu^{\max} &= \frac{E_{\text{meson}}}{m_{\text{meson}}} \frac{m_{\text{meson}}^2 - m_\mu^2}{2m_{\text{meson}}} \left(1 + \frac{|\vec{p}_{\text{meson}}|}{E_{\text{meson}}} \right) \\ &\simeq \frac{m_{\text{meson}}^2 - m_\mu^2}{2m_{\text{meson}}} (E_{\text{meson}} + |\vec{p}_{\text{meson}}|). \end{aligned}$$

It may be noted that the different neutrino energies may be obtained by varying the lifetime and the Lorentz boost (γ_{meson}) of the mesons. Figure 17.17 shows the neutrino fluxes which could be obtained at various accelerators in 1973. This figure has been taken from Ref. [294]. Using modern day accelerators, two different types of neutrino beams are obtained. One is known as the wide band beam and the other is known as the narrow band beam.

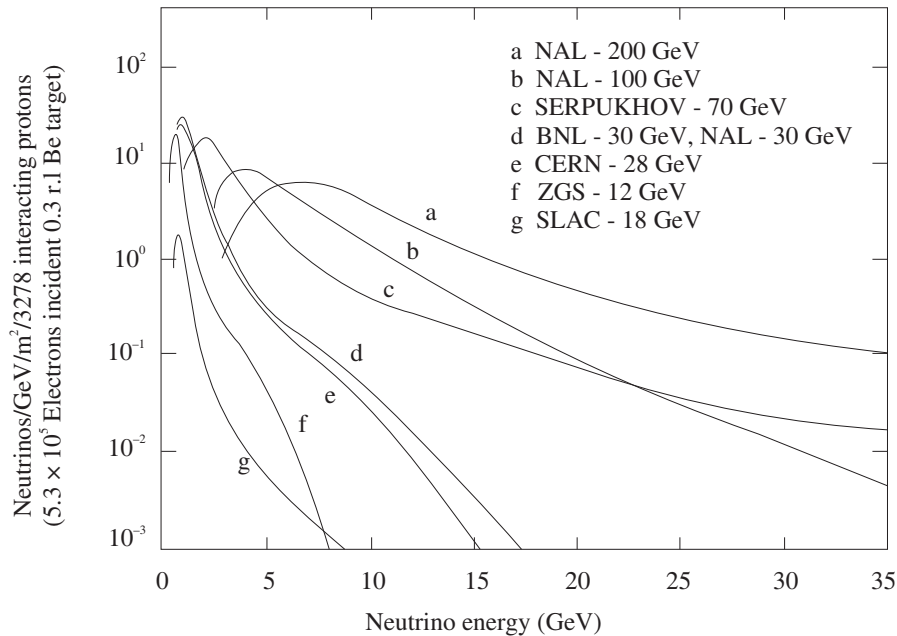


Figure 17.17 Flux of neutrinos from the older generation accelerators [294].

17.8.1 Wide and narrow band of neutrino beams

In a beam of primary protons, the intensity of the beam depends upon the accelerator's performance. To achieve maximum intensity, the produced pions and kaons are to be focused and independent of the energies which they were produced. In this case, a cylindrical target struck by the protons is aligned with the decay tunnel and magnetic horns are placed to focus the mesons (Figure 17.18). Mesons decay in the decay pipe to give neutrinos; the neutrino beam so obtained is known as the wide band beam. In such beams, the energy spectrum and the fraction of different neutrino species can be varied by

- (i) tuning the focusing system by altering the shape of the horn and using different horns in cascade, and
- (ii) altering the length of the decay tunnel, which affects the decay directions of pions and kaons of different energies differently.

The drawback with a wide band beam is that it is very difficult to precisely estimate the energy spectrum and concentrate (relative amount) on the different neutrino species in the beam.

Modern day accelerators providing the neutrino and antineutrino fluxes, are available at the Fermilab in USA, JPARC in Japan, CERN in Geneva, etc. In Figure (17.19), we show the ν_μ and $\bar{\nu}_\mu$ spectra at the Fermilab which have been used by the MiniBooNE collaboration and in Figure 17.20, the low energy spectra being used by the MINERvA collaboration is shown.

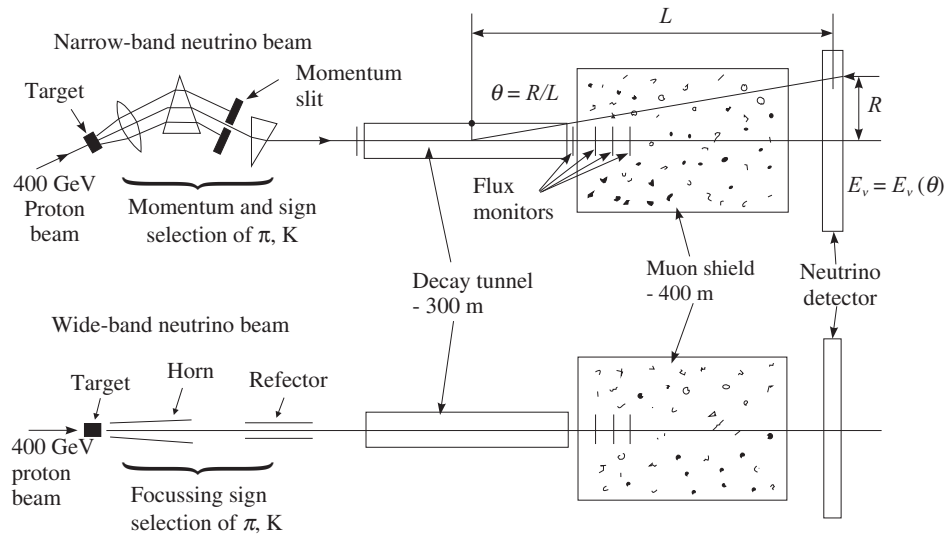


Figure 17.18 Set up for the narrow band beam (top) and wide band beam (bottom).

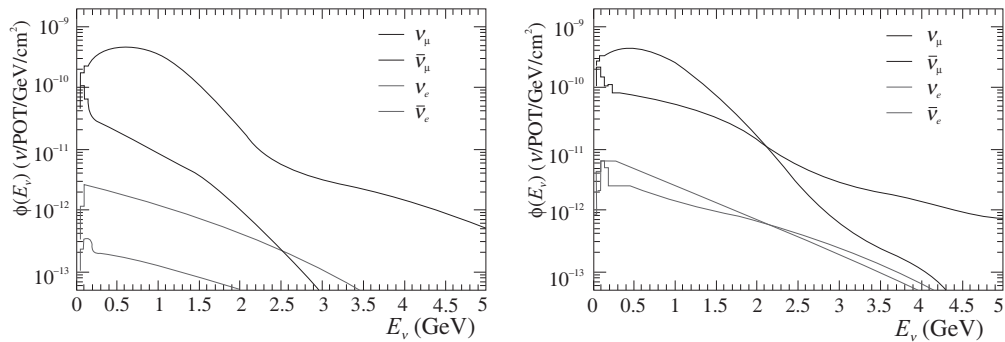


Figure 17.19 MiniBooNE spectra [948] for neutrino (ν_μ) (left) and antineutrino ($\bar{\nu}_\mu$) (right).

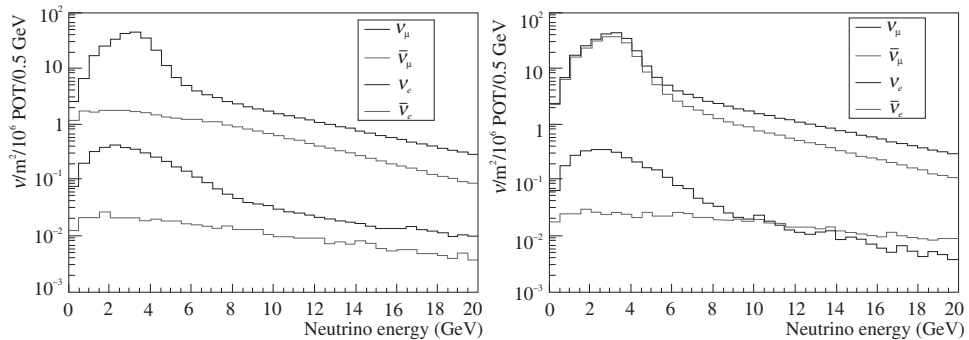


Figure 17.20 MINERvA spectra [949] for low energy neutrino (ν_μ) (left) and antineutrino ($\bar{\nu}_\mu$) (right).

The name narrow band neutrino beam refers to the selection of parent mesons in a narrow energy interval. In this case, the cylindrical target struck by the protons is not aligned with the decay tunnel and additional dipole magnets and momentum slits select the mesons of desired energy (Figure 17.18). The neutrino beam so obtained is also known as an off axis beam. Since mesons of a specific band of energies and momenta are selected, the neutrino fluxes are lesser in intensity compared to the flux obtained through an on-axis arrangement.

The angular dependence of the neutrino energy is obtained by using the four-momentum conservation rule, that is,

$$\begin{aligned}
 p_{\text{meson}} &= p_\nu + p_\mu \\
 p_\nu^2 &= p_{\text{meson}}^2 + p_\mu^2 - 2p_{\text{meson}} \cdot p_\mu, \text{ leading to} \\
 E_\nu &= \frac{m_{\text{meson}}^2 - m_\mu^2}{2(E_{\text{meson}} - |\vec{p}_{\text{meson}}| \cos \theta_\nu)} \\
 &= \frac{m_{\text{meson}}^2 - m_\mu^2}{2|\vec{p}_{\text{meson}}| (1 - \cos \theta_\nu) + \frac{m_{\text{meson}}^2}{|\vec{p}_{\text{meson}}|}} \\
 &= |\vec{p}_{\text{meson}}| \frac{m_{\text{meson}}^2 - m_\mu^2}{m_{\text{meson}}^2 + |\vec{p}_{\text{meson}}|^2 \theta_\nu^2} \text{ (for small angle scattering)} \\
 E_\nu(\theta_\nu) &= E_{\text{meson}} \frac{m_{\text{meson}}^2 - m_\mu^2}{m_{\text{meson}}^2 + E_{\text{meson}}^2 \theta_\nu^2} \text{ (for } E_{\text{meson}} \approx |\vec{p}_{\text{meson}}|) \\
 &\simeq E_{\text{meson}}^{\text{max}} \frac{1}{\gamma_{\text{meson}}^2 \theta_\nu^2} \quad (17.39)
 \end{aligned}$$

Thus, for small angles ($\theta_\nu < 1$) and relativistic mesons ($\gamma_{\text{meson}} \gg 1$), we may write:

$$E_\nu \simeq \frac{m_{\text{meson}}^2 - m_\mu^2}{m_{\text{meson}}^2 (1 + \gamma_{\text{meson}}^2 \theta_\nu^2)} E_{\text{meson}}, \quad (17.40)$$

leading to neutrino flux

$$\Phi_\nu \simeq \frac{1}{\pi L^2} \left(\frac{E_{\text{meson}}}{m_{\text{meson}}^2} \right)^2 \frac{1}{(1 + \gamma_{\text{meson}}^2 \theta_\nu^2)^2}, \quad (17.41)$$

where L is the detector distance. It may be noted that for a detector which is off-axis, the neutrino energy is no longer proportional to the pion energy but rather has a broad maximum for $\gamma_{\text{meson}} \theta_\nu = 1$. The maximum neutrino energy is $\frac{E_{\text{meson}}^{\text{CM}}}{\theta_\nu}$, which therefore depends only on the value of the off-axis angle. Although the flux obtained from mesons in the off-axis beam is smaller than the flux obtained from the on-axis beam, the advantage is that all the mesons in a broad energy range contribute neutrinos in a narrow energy interval around $E_{\text{max}} = \frac{29.8 \text{ MeV}}{\theta}$ for the pions and $E_{\text{max}} = \frac{235.5 \text{ MeV}}{\theta}$ for the kaons. Due to this, the neutrino flux at peak is much larger than that of the on-axis beam at the same energy. Figure 17.21, shows the neutrino spectrum obtained using an on-axis arrangement and also for different off-axis angles for the T2K experiment [904].

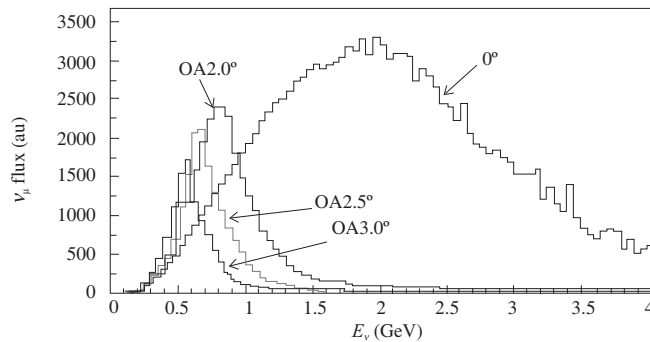


Figure 17.21 Neutrino spectrum for on-axis and different off-axis angles obtained by the T2K experiment [904].

Some of the accelerators which have been used in the neutrino experiments for both wide and narrow beams have been listed in Table 17.7. The various experiments performed using accelerator beams have been listed in Table 17.8 and Table 17.9, for the short baseline and long baseline experiments, respectively.

Table 17.7 List of accelerators.

Lab	Year	p_0 (GeV/c)	Protons Pulse (10^{12})	$\langle E_\nu \rangle$ (GeV)	Experiments
BNL	1962	15	0.3	5	Spark Ch. Observation of 2 ν s
CERN	1963	20.6	0.7	1.5	HLBC, spark ch.
CERN	1969	20.6	0.63	1.5	HLBC, spark ch.
ANL	1969	12.4	1.2	0.5	Spark Chamber
ANL	1970	12.4	1.2	0.5	12' BC
CERN	1972	26	5	1.5	GGM, Aachen-Pad.
FNAL	1974	300	10	50, 180	CITF, HPWF, 15' BC
FNAL	1975	300, 400	10	40	HPWF
FNAL	1975	300, 400	10	50, 180	CITF, HPWF
BNL	1976	28	8	1.3	7' BC, E605, E613, E734, E776
FNAL	1976	350	13	100	HPWF, 15' BC
CERN	1977	350	10	50, 150	CDHS, CHARM, BEBC
CERN	1977	350	10	20	GGM, CDHS, CHARM, BEBC
IHEP	1977	70	10	4	SKAT, JINR
FNAL	1979	400	10	25	15' BC
BNL	1980	28	7	3	7' BC, E776
CERN	1983	19	5	1	CDHS, CHARM
FNAL	1991	800	10	90, 260	15' BC, CCFRR
CERN	1995	450	11	20	NOMAD, CHORUS
FNAL	1998	800	12	70, 180	NuTeV exp't
KEK	1998	12	5	0.8	K2K long baseline osc.
FNAL	2002	8	4.5	1	MiniBooNE
FNAL	2005	120	32	4-15	MINOS, MINERvA
CERN	2006	450	50	20	OPERA, ICARUS
FNAL	2009	120	70	2	NOvA off-axis
JPARC	2009	40	300	0.8	Super K off-axis

Table 17.8 Accelerator (short baseline) neutrino detectors.

Experiment	Reaction	Active mass (ton) & detector	Location (MeV)	Period
CHARM I CHARM II	$\bar{\nu}_\mu A \rightarrow \bar{\nu}_\mu \mu^+ \mu^- A$	692-glass calorimeter	CERN	1979–1984 1986–1991
CHORUS	$\nu_\tau N \rightarrow \tau^- X$	800 kg nuclear emulsion	CERN	1994–1997
LSND	$\bar{\nu}_e + p \rightarrow e^+ n$ $np \rightarrow d\gamma$	167 LS	Los Alamos, USA	1993–1998
NOMAD	$\nu_\tau N \rightarrow \tau^- X$	2.7	CERN	1995–1998
KARMEN	$\bar{\nu}_e + p \rightarrow e^+ n$	65000 liter LS	ISIS, UK	1990–2001
MiniBooNE	$\nu_\mu \rightarrow \nu_e$	800 Mineral oil	Fermilab, USA	2002–2017
MicroBooNE	$\nu_e(^{40}\text{Ar}, ^{40}\text{K})e^-$	170 LAr-TPC	Fermilab, USA	2002– Present
ICARUS	$\nu_e(^{40}\text{Ar}, ^{40}\text{K})e^-$	600 LAr	Gran Sasso, Italy	Future
SBND	$\nu_e(^{40}\text{Ar}, ^{40}\text{K})e^-$	112 LAr-TPC	Fermilab, USA	Future

Table 17.9 Accelerator (long baseline) neutrino detectors.

Experiment	Reaction	Active mass (ton) & detector	Location	Period
K2K	$\nu_\mu n \rightarrow \mu^- p$	1000 (near) 50000 (far) water Cherenkov	KEK to Kamioka, Japan	1999–2004
ICARUS- T600	$\nu_e(^{40}\text{Ar}, ^{40}\text{K})e^-$	760 LArTPC	CERN to Gran Sasso, Italy	2010–2013
MINOS	$\nu_\mu + \text{nucleus} \rightarrow \mu^- + X$	5400	Illinois & Minnesota, USA	2005–2012
NOvA	$K \rightarrow 2\pi/3\pi$ $\pi^+ \rightarrow \mu^+ + \nu_\mu$ $\mu^+ \rightarrow e^+ + \nu_e + \bar{\nu}_\mu$	14000 (far) 300 (near) LS	Fermilab Ash river, USA.	2011–2015
T2K	$\bar{\nu}_e p \rightarrow e^+ n$ $\nu_e e^- \rightarrow \nu_e e^-$	Cherenkov	Tokai to Kamioka, Japan	2013– Present
ICARUS	$\nu_e(^{40}\text{Ar}, ^{40}\text{K})e^-$	600	Gran Sasso, Italy	Future
DUNE	$\nu_e(^{40}\text{Ar}, ^{40}\text{K}^*)e^-$	68000 LAr-TPC	Homestake Mine, USA	Future
T2HK		374000 Water	Tokai to Hyper-K, Japan	Future

17.9 Neutrinos from the Decay at Rest (DAR) Sources

The particles decay at rest (DAR) can provide high intensity, high purity and a well understood flux mainly in the low energy region (Figure 17.22). Various sources which have been discussed in literature to obtain neutrinos are:

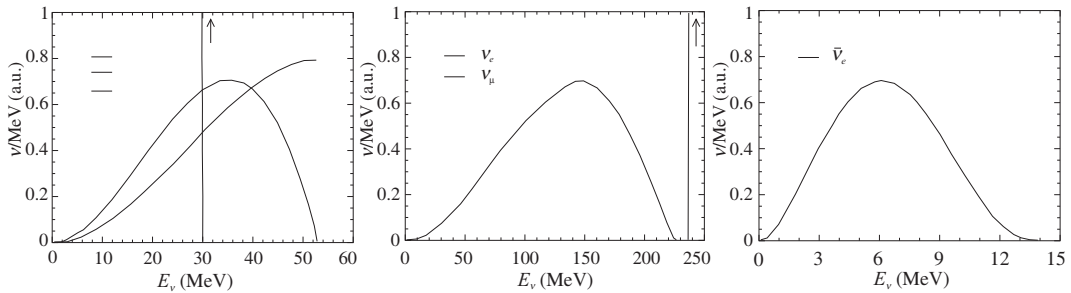


Figure 17.22 Neutrino spectrum obtained from the various sources when at rest: π and μ DAR (left), KDAR (center) and IsoDAR (right).

- Pion decay at rest (π DAR): $\pi^\pm \longrightarrow \mu^\pm + \nu_\mu(\bar{\nu}_\mu)$.
- Muon decay at rest (μ DAR): $\mu^\pm \longrightarrow e^\pm + \nu_e(\bar{\nu}_e) + \bar{\nu}_\mu(\nu_\mu)$.
- Kaon decay at rest (KDAR): $K^\pm \longrightarrow \mu^\pm + \nu_\mu(\bar{\nu}_\mu)$.
- Isotope decay at rest (IsoDAR): ${}^A_Z X \longrightarrow {}^A_{Z-1} Y + e^- + \bar{\nu}_e$.

The two-body decay modes of the mesons provide a beam of monoenergetic $\nu_\mu(\bar{\nu}_\mu)$. The two-body leptonic decay mode of the charged kaon decay at rest (KDAR), that is, $K^+ \rightarrow \mu^+ \nu_\mu$, with a branching ratio of $63.55 \pm 1.1\%$, provides a unique and important source of monoenergetic muon neutrinos of energy 236 MeV. These neutrinos may be used to make high precision measurements of neutrino–nucleus cross sections for the charged current (CC) induced weak quasielastic (QE) production of muons from various nuclear targets. The high precision neutrino–nucleus cross sections measured with a well-defined monoenergetic beam of muon neutrinos may serve as a benchmark for validating many theoretical models currently being used to describe the nuclear medium effects in QE reactions, and which are relevant for the analysis of present day neutrino experiments in the low energy region of a few hundred MeV. These KDAR neutrinos are proposed to be used as a probe to study the new neutrino oscillation modes to sterile neutrinos, that is, ν_μ to ν_s , by performing the oscillation experiments in ν_μ to ν_μ disappearance mode and studying the CC interactions of ν_μ with nuclei, and/or performing the oscillation experiments in ν_μ to ν_e appearance mode and studying the CC interaction of ν_e with nuclei.

KPipe is an experiment which aims to study muon neutrino disappearance for a sensitive test of the $\Delta m^2 \sim 1 \text{ eV}^2$ anomalies, possibly indicative of one or more sterile neutrinos. This experiment is planned to be located at the J-PARC Material and Life Science (MLS) experimental facility's spallation neutron source. Presently, this is the world's most intense

source of monoenergetic (236 MeV) muon neutrinos from the charged kaon decay at rest [950]. KPIPE plans to use a long, liquid scintillation based detector, which would be oriented radially with respect to an intense source of monoenergetic 236 MeV ν_μ s. IsoDAR is a proposed experiment at KamLAND, mainly focussed to study the disappearance of the electron type antineutrinos and to search for the possible existence of sterile neutrinos. The target is to use the high intensity ^8Li β -decay at rest. DAE δ ALUS is a proposed decay at rest experiment for studying CP violation in the leptonic sector. The plan is to use the IsoDAR proton beam as an injector to produce higher energy neutrinos through a stopped pion beam. This source will produce both muon and electron neutrinos as well as muon antineutrinos. The muon antineutrinos will then oscillate to produce electron antineutrinos, whose appearance may be measured and compared to expectation which can be observed in appearance channels.

17.10 Neutrinos from Spallation Neutrons

The low energy neutrino beams ($E_\nu \leq 52.8$ MeV) are generally obtained from the muons decaying at rest. The neutrino energy spectrum obtained from the muons decaying at rest is given by

$$\phi(E_{\nu_e}) = \frac{12}{E_0^4} E_{\nu_e}^2 (E_0 - E_{\nu_e}), \quad E_0 = 52.8 \text{ MeV}. \quad (17.42)$$

This is known as the Michel spectrum and is shown in Fig. (17.22). The neutrino energy spectrum and its energy range is similar to the energy spectrum and energy range of neutrinos coming from the core collapse in a supernova. This similarity in the energy range and spectrum of the supernova neutrinos with the muons decaying at rest, opens up the possibility of connecting the ground based neutrino nuclear experiments with the study of neutrino nuclear cross sections in a supernova. Such a study will also be useful in understanding the r-process nucleosynthesis leading to the formation of heavy elements in the interstellar medium.

Low energy neutrino beams can also be obtained at the Spallation Neutron Source (SNS) facilities, where low energy neutrino reaction experiments can be performed on the nuclear targets to study the selective nuclear transitions. Since SNS produces pulsed neutron beams, the neutrinos are also pulsed, enabling easy separation of signals from the background. The idea behind an SNS facility is to get neutrons when a highly intense beam, for example, at SNS in ORNL, USA, 10^{14} protons of 1 GeV energy are bombarded on a liquid mercury target, in 700 ns wide bursts, with a frequency of 60 Hz. These neutrons then thermalize in hydrogenous and helium moderators surrounding the target before they are delivered to neutron scattering instruments. Besides neutrons, the interactions of the proton beam in the mercury target also produces pions which are stopped inside the dense mercury target before decaying and producing neutrinos. The flux of the neutrinos is quite high $\approx 2 \times 10^7$ neutrinos/cm²/s for the three flavors of neutrinos at a distance of 20 m from the spallation target. The neutrino spectra are monoenergetic for ν_μ and continuous for ν_e and $\bar{\nu}_\mu$ as shown in Figure 17.22. Out of these flavors of neutrinos, ν_e produces electrons which are observed to study the neutrino–nucleus

cross sections for charged current reactions. At ORNL, the COHERENT experiment has recently used neutrinos from the SNS source to study the coherent elastic neutrino–nucleus scattering (CE ν NS) from a target using cesium iodide scintillator crystal doped with sodium to increase the prominence of light signals from neutrino interactions [951]. This is a pioneering experiment which has measured for the first time the coherent ν -nucleus scattering, a process of great significance in astrophysics.

17.11 Neutrinos from Muon Storage Ring (MSR)

Beams of $\bar{\nu}_e$ and $\bar{\nu}_\mu$ are produced from the decay of stored μ^\pm beams. Koshkarev [952], in 1974, first discussed the idea of neutrino production using muon storage ring. In 1980, Neuffer [953] gave a detailed description of a muon storage ring as a neutrino source for doing neutrino oscillation experiments.

Protons of 80–120 GeV energy are used to produce pions off a conventional solid target. The pions are then focused with the help of a magnetic horn and quadrupole magnets. The pions are transported to a chicane (a double bend for sign selection). The pions that decay in the first straight section of the ring can yield muons, which are captured in the ring. The circulating muons then subsequently decay into electrons and neutrinos (Figure 17.23). The nuSTORM facility has been designed to deliver beams of $\nu_e(\bar{\nu}_e)$ and $\nu_\mu(\bar{\nu}_\mu)$. A detector located at a distance of about 2 km from the end of one of the straight sections will be able to make sensitive searches for the existence of sterile neutrinos [954, 955].

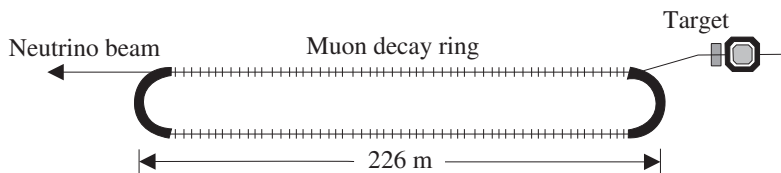


Figure 17.23 Schematic diagram of a muon storage ring.

17.12 Beta-beam Neutrinos

The pure sources of electron neutrinos or antineutrinos from β -beams were first proposed by Zucchelli in 2002 [956]. The idea is to obtain ν_e and $\bar{\nu}_e$ beams through the β -decay of accelerated radioactive ions circulating in a storage ring. These ions would be produced by intense radioactive sources. The β -beams provide a source of pure single flavor, well collimated and intense (anti)neutrino beams with a well-defined energy spectrum obtained from the β -decay of accelerated radioactive ions boosted by a suitable Lorentz factor γ . The radioactive ion and the Lorentz boost factor γ can be properly chosen to provide low [957, 958], intermediate, and high energy [959] neutrino beams according to the needs of a planned experiment.

In the feasibility study of β -beams, ${}^6\text{He}$ ions with a Q value of 3.5 MeV and ${}^{18}\text{Ne}$ ions with a Q value of 3.3 MeV are considered to be the most suitable candidates to produce antineutrino and neutrino beams. The possibility of accelerating these ions using the existing CERN-SPS, up to its maximum power enabling it to produce β -beams with $\gamma = 150$ (250) for ${}^6\text{He}$ (${}^{18}\text{Ne}$) ions has been discussed in literature [960]; this may be used to plan a baseline neutrino experiment at $L = 130$ km to the underground Frejus laboratory with the 440 kT water Cherenkov detector [959]–[961]. The feasibility of such an experimental setup and its response to β -beam neutrinos corresponding to various values of the Lorentz boost factor γ has been studied by Autin et al. [962]. In high γ range, this provides greater sensitivity to the determination of the mixing angle θ_{13} and the CP violating phase angle δ [963]. In addition, such a facility is also expected to provide the low energy neutrino nuclear cross sections corresponding to very low γ , which may be useful in calibrating various detectors planned for the observation of supernova neutrinos [957, 964] and neutrinoless double β -decay [958].

The energy spectrum of β -beam (anti)neutrinos from an ${}^{18}\text{Ne}$ (${}^6\text{He}$) ion source in the forward angle ($\theta = 0^\circ$) geometry corresponding to the Lorentz boost factor γ is given by [965]:

$$\begin{aligned}\Phi_{\text{lab}}(E_\nu, \theta = 0) &= \frac{\Phi_{\text{cm}}(E_\nu \gamma [1 - \beta])}{\gamma [1 - \beta]}, \\ \Phi_{\text{cm}}(E_\nu) &= b E_\nu^2 E_e p_e F(Z', E_e) \Theta(E_e - m_e).\end{aligned}\quad (17.43)$$

In this equation, $b = \ln 2 / m_e^5 f t_{1/2}$ and $E_e (= Q - E_\nu)$, p_e are the energy and momentum of the outgoing electron, Q is the Q value of the β -decay of the radioactive ion $A(Z, N) \rightarrow A(Z', N') + e^- (e^+) + \bar{\nu}_e (\nu_e)$, and $F(Z', E_e)$ is the Fermi function. In Figure 17.24, we show the representative spectra for (anti)neutrinos corresponding to the Lorentz boost factor $\gamma = 250$ (150).

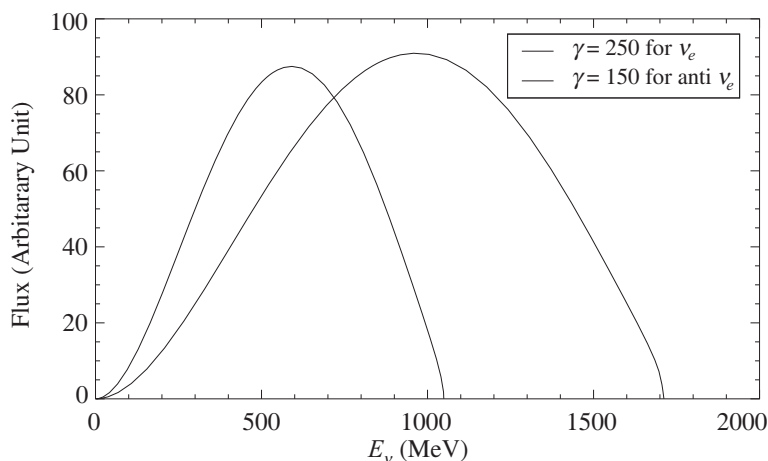


Figure 17.24 Neutrino (solid line) energy spectrum obtained with ${}^{18}\text{Ne}$ boosted at $\gamma = 250$ and antineutrino (dashed line) energy spectrum obtained with ${}^6\text{He}$ boosted at $\gamma = 150$.

17.13 Very High Energy Cosmic Neutrinos

Cosmic neutrinos are very important probes to learn the fundamental physics beyond the TeV scale [966]. The energy scale which can be achieved with cosmic sources at the surface of the earth, is well beyond the energy available from solar neutrinos, atmospheric neutrinos, supernova neutrinos, reactor antineutrinos, or even with the present accelerators (Figure 17.25).

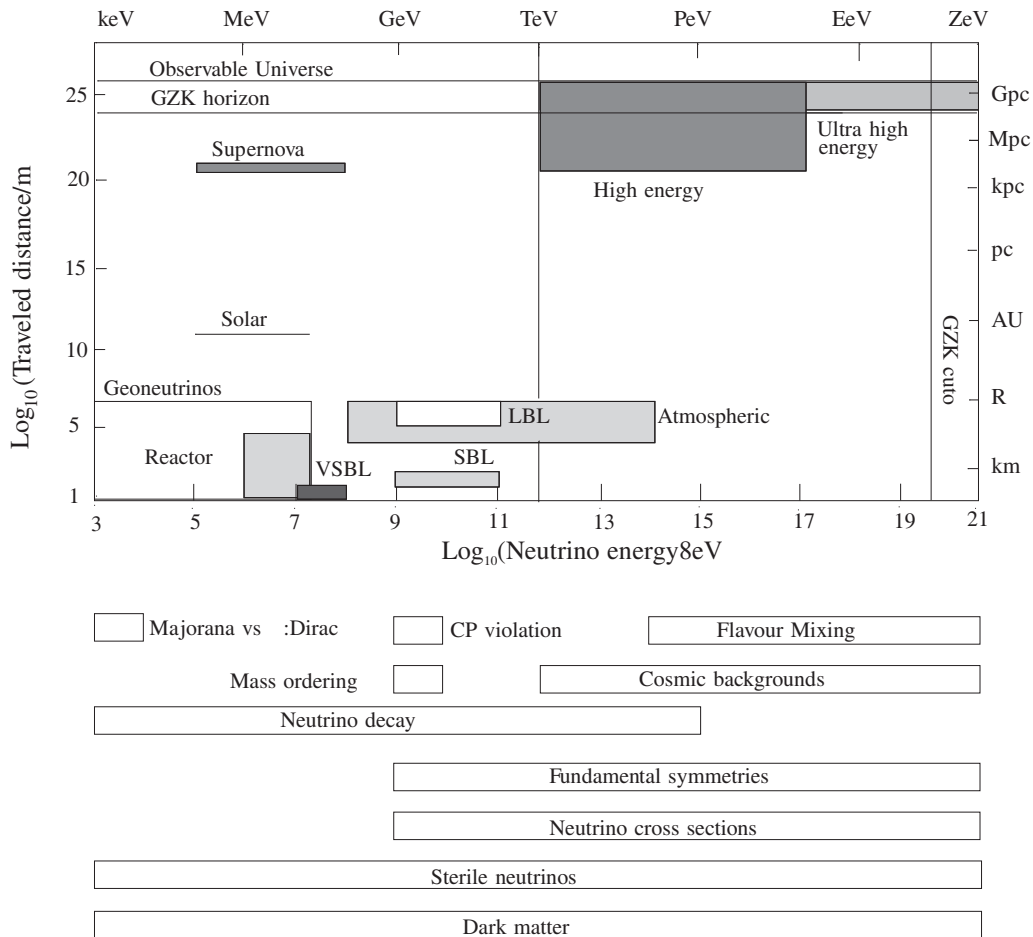


Figure 17.25 Tests of fundamental physics accessible with neutrinos of different energies [966].

At the EeV scale, cosmogenic neutrinos are produced due to the interaction of ultra high energy (UHE) cosmic rays with the cosmic microwave background radiations through the Greisen–Zatsepin–Kuzmin (GZK) effect. When an ultra high energy proton, produced in some far away astrophysical object like a black hole accreting matter, scatters off a photon present as CMBR, it produces very high energy pions, that is,

$$p + \gamma \rightarrow n + \pi^+ . \quad (17.44)$$

The threshold energy required by the proton in the rest frame of the cosmic background radiation is obtained by the following considerations. The temperature of the CMBR is approximately 2.7 K, which corresponds to $235\mu\text{eV}=2.35 \times 10^{-13}\text{GeV}$.

Now, the four-momentum of both the sides of Eq. (17.44), must be the same, that is,

$$\begin{aligned}(p_\gamma + p_p)^2 &= (p_\pi + p_n)^2, \\ \text{at threshold } M_p^2 + 2p_p \cdot p_\gamma &= (M_\pi + M_n)^2.\end{aligned}\tag{17.45}$$

To evaluate $p_p \cdot p_\gamma$, we go to the CM frame, where extremely relativistic protons and photons coming from the opposite direction (say Z-direction), have four-momentum components $p_p = (E_p, 0, 0, E_p)$ and $p_\gamma = (E_\gamma, 0, 0, -E_\gamma)$, respectively, such that $p_p \cdot p_\gamma = 2E_p E_\gamma$, which gives

$$\begin{aligned}M_p^2 + 4E_p E_\gamma &= (M_\pi + M_n)^2 \\ \Rightarrow E_p &= \frac{(M_\pi + M_n)^2 - M_p^2}{4E_\gamma} \\ &\sim 3 \times 10^{20} \text{eV}, \quad \text{using } E_\gamma \approx 2.35 \times 10^{-13} \text{GeV}.\end{aligned}\tag{17.46}$$

GZK limit is a theoretical upper limit on the energy of cosmic ray protons, traveling from other galaxies, through the intergalactic medium, to our galaxy. Moreover, the propagation of neutrinos from the source to the detectors is well understood and predicted by the standard model.

The AMANDA detector located beneath the Amundsen–Scott South Pole station is the largest neutrino telescope running today. It detects neutrinos through their interactions with nuclei of oxygen or hydrogen atoms contained in the ice. The interaction produces a muon and hadronic shower. There is a possibility to observe the very high energy cosmic neutrinos in the coming years. In 2013, the IceCube collaboration announced evidences for the detection of extraterrestrial high energy neutrinos. They have reported the energy range of these neutrinos to be between 30 TeV to 2 PeV [967].

Finally, we summarize in Figure 17.25, the physics goals that could be achieved by the various neutrino sources of different energies.